

Radio Morphology of Giant Quasar 4C34.47



Master Thesis
**Radio Morphology of Giant
Quasar 4C34.47**

By Seyit Höçük
01-09-2006

Supervisor:
Professor Dr. Peter D. Barthel
Kapteyn Astronomical Institute

Abstract

Using VLA data from the archive, the radio morphology of the huge radio-loud Quasar 4C34.47 is investigated. Four images of 4C34.47 were made at two observing frequencies and three array configurations. The images, at resolutions of $\sim 4''$ and $\sim 12''$, reveal an object of 800 kpc in size with a 300 kpc long one-sided jet. An upper limit of the angle to the line of sight of the radio source jet axis was found to be $\lesssim 57^\circ$, confirming that such angles occur even in the largest known Quasars, thereby implying that the effects of relativistic beaming are important in Quasars. No significant depolarization asymmetry was found, suggesting that the extended source has 'outgrown' the intergalactic medium causing such asymmetry.

Contents

1	Introduction	7
1.1	Quasars	7
1.2	Polarization studies	9
1.3	Unification of Quasars and RGs	11
1.3.1	Orientation Preferation	11
1.3.2	Unification with RGs	12
1.4	Giant Quasar 4C34.47	15
1.5	Research Goals	16
2	VLA and AIPS	17
3	Observations	18
4	Methodology of Reduction	20
4.1	Calibration	20
4.2	Imaging	21
4.3	Combining Images	23
5	Summary of Results	24
5.1	High Quality Multi-Resolution Combined Maps	26
5.1.1	Results of Combined Maps	26
5.1.2	Discussion of Combined Maps	27
5.2	Spectral Index of 4C34.47	30
5.2.1	Results of Spectral Index	30
5.2.2	Discussion of Spectral Index	32
5.3	Polarization of 4C34.47	32
5.3.1	Results of Foreground Rotation & Rotation Measure	32
5.3.2	Discussion of Foreground Rotation & Rotation Measure	39
5.3.3	Results of Depolarization Asymmetry	39
5.3.4	Discussion of Depolarization Asymmetry	42
6	Depolarizing Medium	43
7	Properties of the Radio Jet	45
8	Concluding Summary	49

Preface

Begin June 2005, I was searching for a project and a supervisor for my Grootonderzoek, my graduation project. After some looking and asking around, I had a nice chat with professor Peter Barthel and he proposed me a very interesting project.

In the mid 1980's, using VLA data, originally taken by Barthel and colleagues, the radio morphology of the giant Quasar 4C34.47 – then the largest known – was investigated. This Quasar was used as, and still is, a prime test case for the unification scheme of Radio Galaxies and Quasars developed by Barthel and others (Bridle, Garrington and Laing to name a few) in 1988/1989. The imaging data, taken with three different array configurations at two observing frequencies, represent one of the best available data sets on the large scale morphology of a typical double-lobed radio-loud quasi stellar object (QSO). Whereas initial radio images were made, the project was never properly finished.

I jumped at this opportunity and on June 17th of that year, I commenced my Grootonderzoek. Co-adding the datasets, complete analysis and making the ultimate multi-resolution images is the first aim of the project. The implications of the final results constitutes the second part. The analysis focuses on the jet and lobe properties of the Quasar, addressing issues such as jet structure, confinement, orientation, lobe structure and polarization.

In the chapters after the introduction I will explain the methodology used to get the high quality dual-frequency image maps and the combined multi-resolution images. Continuing from this, I analyse the jet structure and polarization properties of the Quasar. I finish my thesis by trying to prove the small angle of 4C34.47 to our line of sight and to see the so-called Laing-Garrington effect, coupled with the ability to say something about the halo and the foreground of this Quasar amongst other things.

1 Introduction

1.1 Quasars

We used to believe that the Universe was a quiet place, slowly settling and without many powerful activities taking place. Our belief was rapidly being smashed into pieces as advances in technology with state-of-the-art instruments opened our eyes to the real monstrous Universe. Not long after seeing a glimpse of the vastness of the Cosmos, realization came that nothing has settled yet; in fact we live in a very active and busy Universe. Tremendous effort was set forth to try to understand all of this and yet there are so many things which we still cannot comprehend. Enthrilling objects like massive black holes, powerful active galaxies, overwhelming explosions and immense radiant sources are not uncommon.

Quasars are amongst the most energetic objects in the heavens. When astronomers first noticed them in the 1960s at radio frequencies, they suspected them to be some peculiar nearby stars. Later on it was discovered that these strange objects were actually a lot farther away and not stars at all. Quasars get their name from the first observation as being radio emitting star-like objects, hence they were called quasi-stellar radio sources, in short Quasars. These structures are in fact very active galaxies. Not all QSOs are detected at radio frequencies though, actually there are now more observed in optical and other frequency regimes.

At the cores of these extravagant sources it is believed that there must lie super massive black holes, that are surrounded by a spinning disks of material which is drawn relentlessly into its gravitational maw. At two opposite outer edges of the core, highly collimated streams of particles can be hurled into space with enormous speeds very close to the speed of light. Optical QSOs do not manifest this feature. How these so-called 'Jets' form, what their properties are and why there are knots within them, no-one can fully answer. Twisting and wrapping of strong magnetic-field lines in the spinning disk cause ions to be accelerated. At the poles, these particles get incredibly collimated by the tightly confined field-lines and shoot outwards at very high speeds. This is the best answer for the streaming radio wave emanating particles coming from the poles which we call jets.



In most cases only on one side a jet has been observed though. The reason for that is because the jet approaching the Earth is relativistically 'beamed' [Pearson and Zensus, 1987]. The radio emission received from the jet at one side is always much brighter than that from the other side. This asymmetry is a consequence of flow speeds approaching that of light. A flow moving towards us at almost the speed of light catches up with its own radiation, which thereby appears boosted in intensity. In contrast, the radiation from a flow moving away from us is correspondingly dimmed, making a fainter "counterjet". Radio emission coming from a Quasar and its jets is due to synchrotron radiation, generated by accelerating electrons to ultra relativistic speeds through magnetic fields. This non-thermal emission provides a wealth of information about the properties and morphology of a Quasar.

Not all Quasars are emitting strong radio waves. In fact, most have very weak radio emission that deserves the name radio-quiet. Radio 'loudness' is a measure for the radio strength of a source and is usually parameterized by R , the ratio between centimeter (radio) to optical flux densities. This parameter is conventionally defined as $R \equiv L_{5GHz}/L_{440nm}$. Generally, the ratio $R = 10$ is chosen as the boundary between the two populations. According to this criterion, only a small fraction of objects $\sim 10\%$ are dubbed radio-loud [Kellermann et al., 1989, 1994, Stocke et al., 1992]. Another criterion is to select the boundary at $P_{6cm} \approx 10^{25} \text{ W Hz}^{-1} \text{ sr}^{-1}$ [Miller et al., 1990]. This also qualifies only 10%-20% of the objects as radio-loud. To be completely objective, it must be noted that there are some studies that are questioning the used distribution where-after Ho and Peng [2001] recalculated the radio-loudness with a different distribution and claim that at least 60% of the sources count as radio-loud.

Just like Quasars, Radio Galaxies (RGs) can be distinguished in the same manner, with the main difference that RGs are optically less luminous compared to Quasars. Perhaps it's better to say that Quasars are the powered-up versions of RGs. In figure (1) you can see an example of a powerful radio-loud RG.

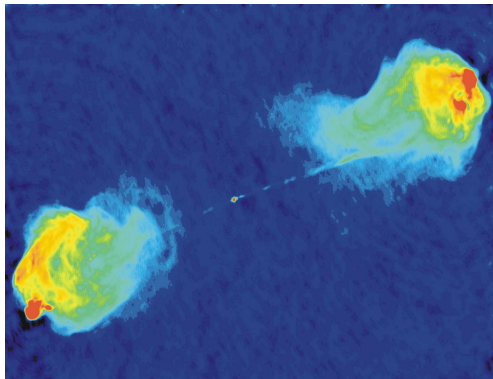


Figure 1: Cygnus-A

On the left side, a false color image of Cygnus-A (3C405.0), the most powerful Radio Galaxy in our part of the universe is shown. At 700 million light years distance, this double-lobed object is one of the brightest radio sources in our sky. It is receding from us at $16811 \text{ km sec}^{-1}$ and corresponding to a redshift of 0.05607. Red in the image represents the regions with the brightest radio emission, while blue shows regions of fainter emission. At its center is a faint galaxy.

Cygnus A is a FRII object as it displays bright hotspots (in contrast to the less powerful FRI's).

Quasars are now known to be the most distant and powerful sources of energy in the Universe. Just now scientists are beginning to unravel the mysteries of this object, but still dazzled by the amount of power shooting out from the core. How the knots are created in the jets, which are like lumpy clouds of gas, is still quite puzzling.

1.2 Polarization studies

Polarization is an intrinsic property of electromagnetic waves. EM-waves have two components which oscillate in the plane perpendicular to the direction of travel: a magnetic and an electric component that are perpendicular to one another. Polarization is the term which describes the direction of the EM-wave's transverse electric field. In general, the directions of these components are distributed randomly in a beam, the EM-wave is then called unpolarized. However, when one direction of oscillation is 'preferred' more above the rest, the wave is dubbed polarized and the amount of polarization is usually indicated in fractions of the total intensity.

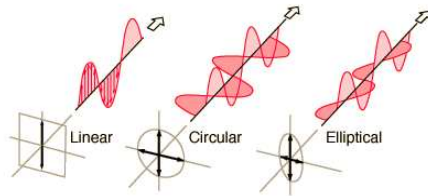


Figure 2: The manifestation of three types of polarization

There are sources that can generate light waves which are partly polarized. It is also possible that an EM-wave comes in contact with a medium where it can get polarized or depolarized. By measuring the direction and strength of polarization at different frequencies and various positions on the source, we can get answers to questions about the manner of generation of waves, its neighbourhood, the foreground and about the orientation of the object. To specify and quantify the phase and polarization of radiation, there are four parameters called the Stokes parameters. These observable quantities I , Q , U and V are operationally defined, but can be mathematically related to the electromagnetic field. Q and U together represent the linearly polarized component, with a 45 degree angle between them. V represents the circularly polarized component and I is a measure of the total power – polarized and unpolarized – of the radiation. With the use of these parameters, the polarization intensity and phase can be easily quantified.

Synchrotron radiation has a number of unique properties. One of them is that it generates highly polarized radiation dependent on the magnetic-field \vec{B} of the surrounding area and these photons are emitted with energies ranging from infra-red to energetic X-rays. This is a great tool for astronomers studying active galaxies. Unfortunately, polarization studies require high resolution observations, because averaging of different polarizations within the beam causes depolarization.

From the polarization properties of Quasars at different frequencies, one of the interesting things that can be studied is the foreground affecting it. Known as the Faraday effect, the plane of polarization of an electromagnetic wave can be rotated under the influence of a magnetic field (parallel to the direction of propagation) within the path of the observer.

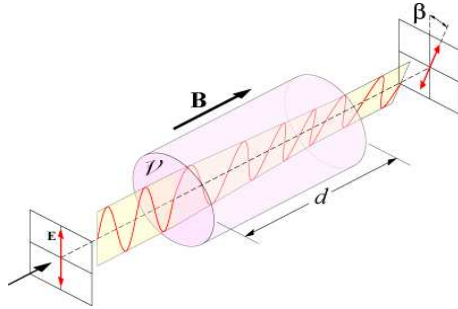


Figure 3: Diagram of the Faraday effect

The amount of rotation β , displayed in figure (3), is given by $RM \cdot \lambda^2$, where λ is the wavelength of the radiation and RM is a factor known as the rotation measure in units of $\text{radians} \cdot \text{m}^{-2}$. RM depends on a number of parameters, see equation (1).

$$RM = \frac{e^3}{2\pi m^2 c^4} \int_0^d n_e \vec{B} \cdot \vec{ds}, \quad (1)$$

\vec{B} , the magnetic flux density in the direction of propagation

n_e , the number density of electrons

d , the length of the path where the light and magnetic field interact

e and m , the charge and mass of an electron

c , the speed of light in a vacuum

Observing Faraday rotation in the radiation from RGs and Quasars are among the most important ways of studying the environment and foreground of these objects.

1.3 Unification of Quasars and RGs

1.3.1 Orientation Preferation

As we know, there are various types of Active Galactic Nuclei (AGN). The optical spectra of different types of AGN is shown in figure (4). These are

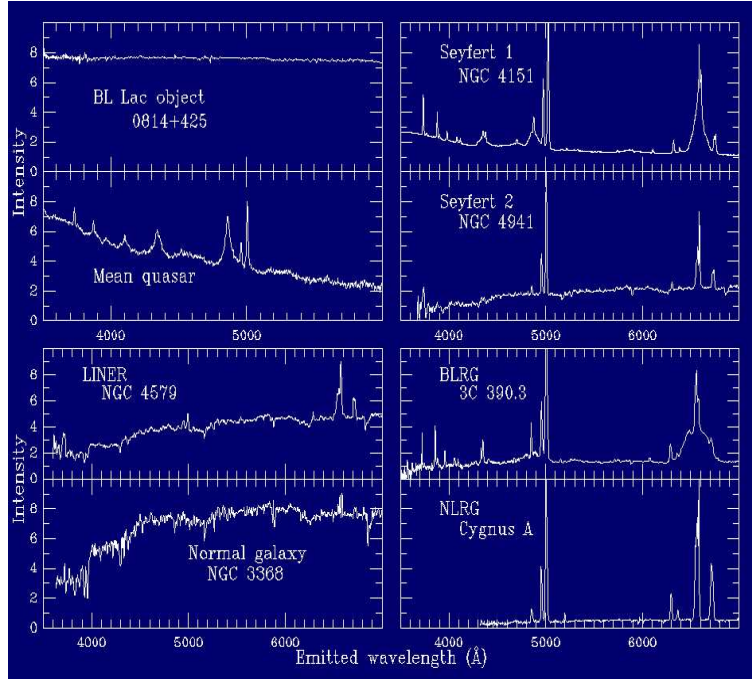


Figure 4: Spectra of eight types of AGN

all seemingly different kinds of complex monsters. The human mind works in such a way that it craves for simplicity, because it is easier for us to understand. Our deepest instincts but also, perhaps more importantly, experiences tells us that everything should start out simple to get more complex in time. This is why we constantly try to find explanations for complex things in simple ways. Unification is an attempt to explain the diversity of observational properties in terms of a simple model.

Active Galactic Nuclei can be unified in multiple ways. Two aspects are generally used to explain differences between the types:

(1)

The existence of an opaque dust torus surrounding the AGN responsible for the broad absorption lines when viewing under certain angles to the object.

(2)

Orientation related effects to explain superluminal velocities and the display of (one-sided) jets.

With these two ingredients, good unification schemes can be postulated. Orientation of the source relative to us plays a major role here. Still, there are many things to be considered. In the second mentioned aspect, if one assumes to find answers for Quasars just by saying these are objects oriented towards us, one has to think about what the parent population should look like. A fitting quote (Barthel 1995): 'There must be parents for beamed or otherwise favourably oriented objects'.

1.3.2 Unification with RGs

Late seventies and early eighties there was much speculation and turmoil about AGN unification. Many had attempted to unify various types of AGN to another with models, however most were rather quickly disproved. In 1978, there was a BL Lac meeting in Pittsburg where the foundations for beaming unification for radio-loud objects was laid. Quasar and RG unification was speculated before, but first published by Barthel [1989]. Barthel proposed a scheme to unify radio-loud FR II Quasars and FR II Radio Galaxies as members of the same population of galaxies observed in systematically different orientation to the line of sight. In his model, the parent population of intrinsically similar AGN are randomly oriented, and the transition from radio-galaxy to Quasar properties should occur around 45 degrees to the line of sight. The idea was deduced from the fact that all the radio-loud Quasars showed single-sided jets together with the observation that too many of them were superluminal. To test this unification scheme, the large double-lobed Quasar 4C34.47 was observed. After detecting high superluminal motion, it showed that even extreme large Quasars can still have substantial angles to the plane of the sky. Though Quasars have strong continuum and broad lines and Radio Galaxies have only faint lines, how could they be the same thing? This can be answered if an optically thick torus is present around the Quasar and depending on the angle we observe, the radiation is blocked at high inclination.

In order to check the unification model one can look at the intensity ratio of the jet compared to the counter-jet. Because we look at the object under an angle, the fluxes of jet and counter-jet differ from one another. The smaller the angle between the two jets relative to our line of sight, the larger the ratio of flux densities S_j/S_{cj} will be.

By looking and comparing the jet-ratio of Quasars versus Radio Galaxies, the prediction that these two only differ in orientation can be proven. RGs should have much smaller flux ratio between the jets. See figure (5) for a comparison between the jets of a RG and a Quasar. Whilst it is hard to make a good comparison as most counter-jets in RGs and moreover Quasars are hard to detect, if detected at all, it is still possible and this has been done by some. Barthel et al. [1989] present a lower limit of 10:1 to the jet ratio for Quasar 4C34.47, which independently proved their preferred orientation.

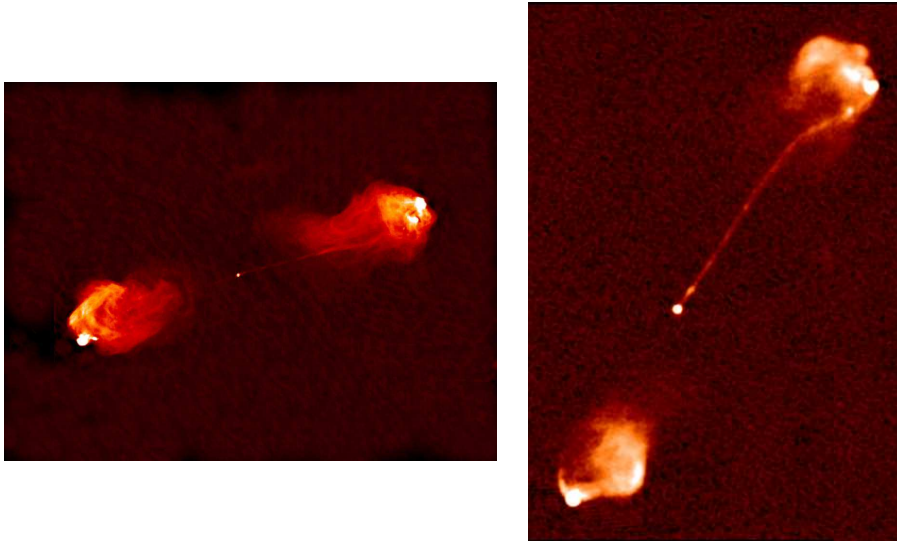


Figure 5: Two images where the jets of the radio sources can be seen. On the left side an image of Radio Galaxy Cygnus A and on the right side the Quasar 3C175 taken from the 3C catalogue of Alan Bridle.

Another approach to test the model is to look at the depolarization asymmetry. Depolarization can occur if there is a magneto-ionic medium around the source which reduces the polarized intensity of the emission, because Faraday rotation on small scales gets averaged within the observed beam. The asymmetry occurs because of a different kind of effect. This because, the lobe that is fed by the brighter jet would also be closer to the observer. This lobe would be viewed along a shorter path through the magneto-ionic medium, and therefore depolarize at a longer wavelength than the other lobe [Laing, 1988, Garrington et al., 1988], see figure (6).

A few more properties with which one can test this model are: core size or core intensity, jet prominence and emission-line gas asymmetry, but these will not be discussed in this report.

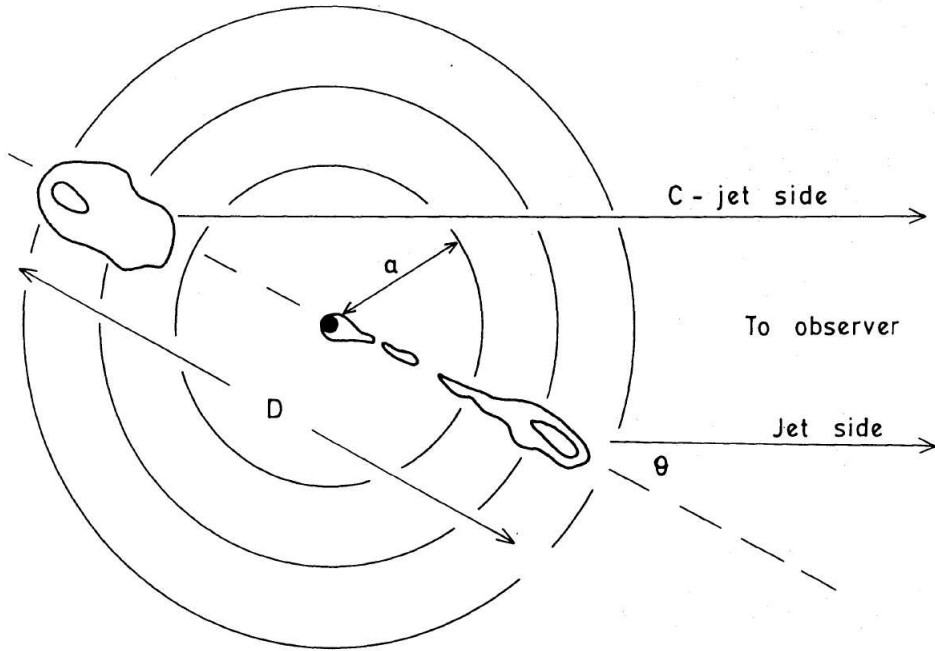


Figure 6: Sketch of the source and a magneto-ionic medium around the source demonstrating the Faraday screen which can cause the depolarization asymmetry. D is the diameter of the screen, a the radius and θ the angle to the line of sight.

1.4 Giant Quasar 4C34.47

The radio source 4C34.47 was around 1987 known as one of the largest objects in the sky. It has an apparent magnitude of 16.5 and is relatively close to us at a redshift (z) of 0.205999 ± 0.000050 [Paturel and Petit, 2002]. Using the most recent and accurate cosmological parameters adopted from WMAP, $H_0 = 73 \text{ km s}^{-1} \text{ Mpc}^{-1}$, $\Omega_M = 0.24$ and $\Omega_\Lambda = 0.76$, it was possible to calculate the luminosity distance D_L of 4C34.47 to be 980 Mpc and a scale size of 3.27 kpc per arcsecond. The absolute V magnitude corresponding to this is -23.5, which makes it fall into the category of a faint but a real Quasar.

This double lobed Quasar is a typical Fanaroff-Riley class II radio source and it has a large angular size. We shall see in this thesis that it is $250''$ in overall angular extent, with a linear size of $817 \text{ kpc} \pm 15 \text{ kpc}$ and that it has a very tight and straight radio jet of $260 \text{ kpc} \pm 15 \text{ kpc}$. Because of this large angular size, it is excellent for multi-frequency radio mapping. The center of 4C34.47 has a variable core which is discovered to be expanding at superluminal speeds (1989). The core is also very bright in relative terms, containing approximately half the flux density of the total source. This is unusually high for lobe dominated sources.

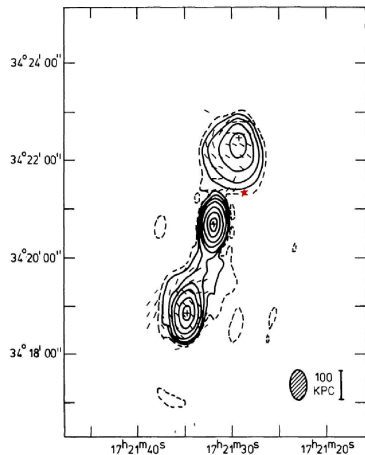


Figure 7: Total intensity contour plot by Jägers et al. 1981.

A contour image made by Jägers et al. [1982] with the WSRT is shown in figure (7). Here you can see the intensive core in between the two hot spots. The size to this precision and the presence of jets were not known at that time. Within this figure, there is another QSO visible, marked by a red star, with a redshift of 1.80 [Hewitt and Burbidge, 1980]. This QSO has no detectable radio emission and is not connected to 4C34.47 in any way.

Suggested by Antonucci and Barvainis [1988] is that there also is an isotropic far-IR component in these sources. The thermal part of this radiation is coming from dust in the central torus and around the host galaxy. Radiation created this way is independent of orientation of the source. But it can also come from synchrotron radiation which is non-thermal in nature, because synchrotron radiation is produced in a wide range of energy levels and since the jets are beamed, the emission is strengthened plus shifted towards shorter wavelengths. These sources of radiation are indeed detected for RGs and QSOs with IRAS (Infrared Astronomical Satellite) [Golombek et al., 1988, Neugebauer et al., 1986].¹

¹Quasar 4C34.47 has also been observed with IRAS and the object was detected (unexpectedly). This is additional evidence for a boosted core.

One of the more unusual things about this source is that it has a H_β emission-line profile with a FWHM of 1800 km s^{-1} [Miley and Miller, 1979, Wills and Browne, 1986]. Going back to figure (4) you can see the Balmer lines ($H_\beta, H_\gamma, H_\delta$) and Oxygen-lines, with the two most prominent lines being of OIII (4959\AA and 5007\AA).

1.5 Research Goals

The aim of my research consists of two parts:

My first goal is to combine VLA datasets of Quasar 4C34.47 with two different resolutions into one ultimate image, i.e. combining images with the same frequency but with different array configurations. The idea is to get a very detailed radio image of 4C34.47 which has never been done before for this source. To achieve this, I will use the data taken with the VLA radio telescopes at two different frequencies with three different array configurations. Reducing these data to make four calibrated images for two different resolutions is the first step. Using these completely calibrated and cleaned images to make two combined dual-resolution images is the next step and will conclude the first goal. Details of the technique will be explained in the next sections.

My second goal is to analyse the properties of 4C34.47 from the images. In order to do this, I will calibrate the data for polarization and examine and discuss the polarization structure of the source. I start analyzing by measuring the spectral index of 4C34.47 and by finding the amount of rotation that the polarization vectors undergo due to the effects of the foreground and accompanied with it, determining the rotation measure at several different locations of this source. The results will allow me to say something about the foreground of this source. I will continue by looking at the depolarization measure and test if there exist any differences between the two sides of the Quasar. If so, this will allow me to see and measure the Laing-Garrington effect. Subsequently, I will also measure the intensity ratios of the jets at the opposite sides of the core. I will compare both results to the predictions made by the unification model. These tests if conform the predictions, will support the unification model.

2 VLA and AIPS

The Very Large Array -located in New Mexico, USA- is an interferometer of 27 radio telescopes. Each radio telescope is 25 meters in diameter. The 27 radio telescopes are positioned in a Y-shape to get good instantaneous coverage of the sky and they can be moved to change the distances between each other. There are 4 different array configurations possible: A, B, C, and D, plus a few intermediate configurations. The longest baseline for each configuration is 36km, 10km, 3.6km and 1km respectively. Its wavelength coverage ranges from $\lambda=0.7$ cm to 400cm (or 74 to 50,000 MHz) with a theoretical maximum resolution of $0.04''$. All of the raw data acquired with VLA are stored in an archive and after 1 year of acquisition, the data are released to the public.



For reduction and analysis of radio astronomy data from VLA, a package called AIPS (Astronomical Image Processing System) is used. AIPS is a software package for calibration and editing of radio interferometric data and for the construction, display and analysis of astronomical images made from those data using Fourier synthesis methods. It is a composition of smaller programs, called 'tasks', within the master program. Each task has its own specific function. With the use of the specific tasks, the data reduction and analysis of this project has been realised.

3 Observations

The project started by selecting the appropriate observational data from the VLA archives. From 1984 there have only been a handful good observations made of Quasar 4C34.47 and four of these are the ones by Van Breugel and Barthel, but the data were not completely analysed. For this research it was required to have long integration times on this source, this was the first criteria. Another criteria was to have observational data of two different resolutions and of each resolution at two different frequencies, making it a total of four observations. Furthermore, the chosen resolutions could not be high or too low. These selections were required because, for the goal of this research it was essential to get detailed information about the jets and its structure where high resolution images are good (especially for polarization), but also for the lobes and diffuse structure where lower resolution gives more information. With these three criteria the selection of choices was greatly reduced. Before eventually choosing for the data taken by Barthel in 1984, two others were tested and rejected; one for low integration times and another for too high resolution and for not having any other data with the same resolution. All of the chosen data were taken in 1984 between January 20 and July 30. These observations were done on different dates due to fact that they were made with three different array configurations and the VLA changes configuration every four months. The two bands in which the observations were made, are the C band (6cm) and the L band (20cm). In table (1) the typical resolutions for the used bands and array configurations are shown.

Table 1: The typical resolutions θ_{HPBW} of the observations in arcseconds.

Configuration	C band	L band
B	n/a	3.9''
C	3.9''	14''
D	14''	n/a

Total integration times for the observations are in the range of 2.5 to 6 hours with alternating 10 to 20 minutes on target, which is the source 4C34.47, and around three minutes on a calibrator. The exact observation times are shown in table (4). Two calibrators have been observed; the Quasar 3C286 and Radio Source 1732+389. The primary calibrator is 3C286 and its main use is for amplitude calibration, but also to correct for the phase difference of right and left polarization. The exact flux and polarization of this source is known for a broad range of frequencies. 1732+389 is the secondary (phase and amplitude) calibrator. Phase calibration is needed to get the exact position of the prime target; the coordinates of 1732+389 are known at milliarcseconds precision. Usually these secondary calibrators are chosen to be in the vicinity of the target source, because observations occur by switching back and forth between the

target source and the phase calibrator. Each observation was made with two intermediate frequencies, from here on called IFs, with the frequency difference between the two IFs being 50 MHz. Coordinates of these sources are shown in table (2).

Table 2: RA and Dec positions of the centers of target and calibration sources in 1950 (FK4) and 2000 (FK5) coordinates.

Source name	Right Ascension (in hours)	Declination (in degrees)
4C34.47 (1950)	$17^h 21^m 32.02^s$	$34^\circ 20' 41.4''$
4C34.47 (2000)	$17^h 23^m 20.80^s$	$34^\circ 17' 58.0''$
3C286 (1950)	$13^h 28^m 49.657700^s$	$30^\circ 45' 58.640000''$
3C286 (2000)	$13^h 31^m 08.287984^s$	$30^\circ 30' 32.958850''$
1732+389 (1950)	$17^h 32^m 40.487500^s$	$38^\circ 59' 46.932000''$
1732+389 (2000)	$17^h 34^m 20.578534^s$	$38^\circ 57' 51.443100''$

4 Methodology of Reduction

4.1 Calibration

All the data are calibrated using standard calibration techniques in AIPS. The intent of calibration is to recover the true visibility. Observed visibilities differ from the true visibilities for a multitude of reasons. By observing sources which are perfectly known in amplitude, phase and polarization, the measurement errors in antennas and baselines are determined. Obtained error information is used on the observed data to find the true visibilities. This whole process is done by first reading the data from the files into AIPS and if necessary combining the raw data which were split up due to the size. After deciding on a reference antenna (defined on having phase = 0), the known flux is set for the primary calibration source. Before starting the calibration steps, the right uv-coverage range, where each calibrator is tuned to, is put into the calibration task in AIPS. These can be found in the VLA calibrator manual. In the first step of calibration, a limit for amplitude and phase errors are chosen. Then the data is calibrated with the primary calibration source and this calibrated data is put into a solution table. Baselines exceeding the maximum error values are 'flagged' and discarded, because severely corrupted data is worse than no data at all. Hereafter, the data is again calibrated for the second calibration source, updating the solution table. Again the exceeding values if any, are flagged. After this calibration step and carefully discarding corrupted data wherever needed, the flux of the second (phase) calibrator is attained. In the final calibration step, the source is calibrated for amplitude and phase by the calibration sources. Again, they are checked for errors and if any were to be found, the whole calibration process was restarted.

A good test to see if everything went correctly, is to make a uv-plot like in figure (8). You can see that there are more points at shorter baselines than at longer baselines. This is logical, because there are much more shorter distances between the telescopes than longer distances. You also see the upper envelope steadily decreasing to longer baselines. Shorter baselines can detect more flux because they have a larger angular scale and cannot resolve the source as good as at the longer baselines. After satisfactory calibration, the images were split to get a single file with only the target source. The important values of calibration for each observation are shown in table (3).

All of the data are also calibrated for their polarization using standard polarization calibration techniques involving antenna polarization calibration. Not only from each data their stokes I, Q and U components are split and crafted into an image, but also each image is separated for both their IF frequencies. A standard image size is chosen to use on all the images for making things simpler later on.

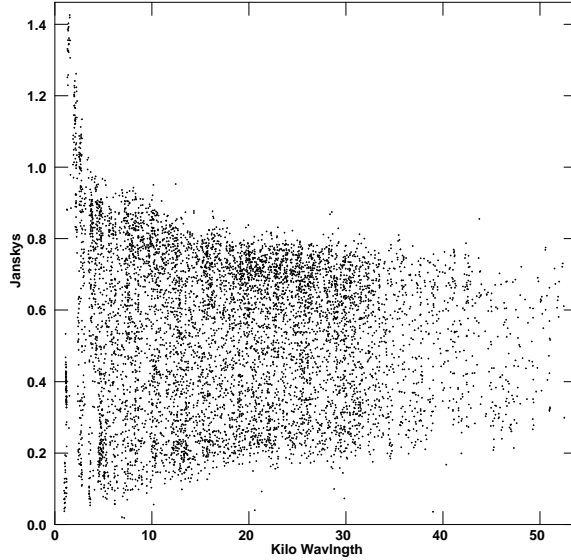


Figure 8: An example uv-plot of an observation of 4C34.47 taken with L-band B-array. X-axis is the baseline length (in $\text{kilo}\lambda$), Y-axis is the flux (in Jansky's).

Table 3: Important values used by calibration.

Obs. Code	My Code	IF-I (GHz)	IF-II (GHz)	Longest Baseline	Ref. antenna	uv-range ($\text{kilo}\lambda$)
AV91	A1	1.4462	1.4962	10km	25	0-18
AV91	A3	1.4524	1.5024	3.6km	2	0-18
AV91	A4	4.8726	4.8226	3.6km	2	0-25
AV112	C12	4.8851	4.8351	1km	16	all

4.2 Imaging

Images are made by setting the best cell size per beamwidth (in arcseconds) to get the highest possible detail and yet still be able to fit the whole data into the chosen image size. All maps are cleaned, i.e deconvolving a sampling function (the "dirty beam") from an observed brightness ("dirty map") of a radio source to reduce the introduced noise in images, using the CLEAN algorithm. To use another algorithm, the maximum entropy deconvolution, was also considered. The conclusion was that there are not many significant differences between the two and that maximum entropy deconvolution gives a slight smoother images but CLEAN gives lower off-source noise and lower zero-level offsets.

Cleaning the images is done by finding out the best technique and steering this to get the best results. This technique is a step by step method starting with cleaning the images using maximum gain and low number of iterations to get an intermediate map. This step is followed by self-calibration with all of the first set of positive clean components of this previously cleaned map. In a few cases, only the clean components within a selected box are used to get even better self-calibration. When doing this, the used solution interval is set to two minutes of the sampled data. Now starting back from the beginning, the latest self-calibrated map is again cleaned but with a slightly lower gain and with an increased number of iterations. Thus, the whole process is cycled through a cleaning step and a calibration step. With each cycle the gain is lowered and the number of iterations is increased. After a few cycles the image already shows much improvement, almost to its limit. The theoretical sensitivity limit that can be achieved are listed in table (4). Most calibrations are done by calibrating with the 'phase only' solution. The Clark clean process factor which by slowing down the cleaning process causes deeper clean in each major cycle, is used in order to improve results. Slowing down the process does not affect the outcome that much, though every little bit of improvement helps. Another parameter which is used for improvement, is the robustness parameter. With this, you can choose to distribute the weights differently between short and long baselines and is useful when you want to highlight areas of the image. On a few occasions, instead of using the robustness parameter, self-calibration is done with a selected uv-range (10-30 $k\lambda$) to reduce the noise to a minimum. Finally, an 'amplitude' solution of self-calibration is applied. In the end of all the cycles, one final deep cleaning is done with 10.000 and up to 120.000 iterations.

Table 4: Integration times with theoretical noise and the maximum sensitivity limit achievable for each observation

Code	Observation time (minutes)	Time on Source (minutes)	VLA theoretical Sensitivity RMS (10 min) (mJy)	Sensitivity limit (per observation) (mJy)
A1	145	106.5	0.056	0.0172
A3	164	118.5	0.056	0.0163
A4	263.5	191	0.054	0.0124
C12	342.5	93	0.054	0.0177

4.3 Combining Images

Completely calibrated and cleaned images are combined for multi-resolution imaging. Removal of the cores before combining is needed because this Quasar is known to have a variable core. Two images with different core intensities cannot be put together. This is circumvented by first selecting a box around the core and then making an image of this core just to find out the clean components within. With the use of these clean components, the core is then subtracted from the total image. After subtracting the core from 2 different resolution images and calibrating the images once more, the uv-datasets are concatenated into one. Hereafter, one of the removed cores is then put back into the data. The combined images are then again fully cleaned.

5 Summary of Results

All the results are deduced from the images that were made from the VLA observation data. These images are shown in figure (9). A codename is given to each image as previously stated in table (3). The high resolution images (A1 & A4) show details of the jets, while in the relatively low resolution images (A3 & C12) the diffuse structure is better seen. In table (5), the observational parameters are listed. Inferred from the image, we can see that the measured noise as listed in this table, is comparable to the theoretical noise. Because the half power width of the primary beam is comparable to the source size at these frequencies, there might be the problem of primary beam attenuation. Though this could have been corrected by slightly mispointing the telescopes inadvertently, it was deemed unnecessary. Each telescope has a diameter of 25 m; this gives a primary beam width at 6 cm of $R \simeq 1.22 \cdot \lambda/D \simeq 586''$ which equals $9.8'$. As can be seen from the images, the source has an approximate size of $\sim 4.5'$. Therefore, not much concern is needed for this problem.

Table 5: Observational parameters.

Code name	Frequency (GHz)	Conv size RA x Dec (arcsec)	Maximum (mJy Beam ⁻¹)	RMS Noise (mJy Beam ⁻¹)
A1	1.47115	4.60 x 3.83	477.7969	0.0800
A3	1.47740	12.56 x 11.72	489.3008	0.1066
A4	4.84760	4.75 x 4.61	339.5345	0.0419
C12	4.86010	12.96 x 12.83	337.1731	0.0546

From the first view on the maps, we see that both the hot spots, the core and the jets from one end to the other are in a straight line. The southern hot spot is brighter than his northern companion but the core is the brightest. From the magnetic poles of the core, astonishingly collimated streaming particles are the cause for the existence of jets. Only one side, the side coming towards us, is visible though. No counter-jet has been observed. Perhaps even more astounding are the knots within the southern, front jet, that show as areas of high radio intensity. It is unknown why these anomalies exist. It has been argued that perhaps there are objects along the path of the jet with a magnetic field or shock waves causing the particles to emit more synchrotron radiation.

The intensity of the core is quite high. Relative to the total intensity, the core contributes $\sim 30\%$ – 40% for 20 cm observations and for 6 cm maps this percentage is higher $\sim 55\%$ – 60% due to the different radio spectra.

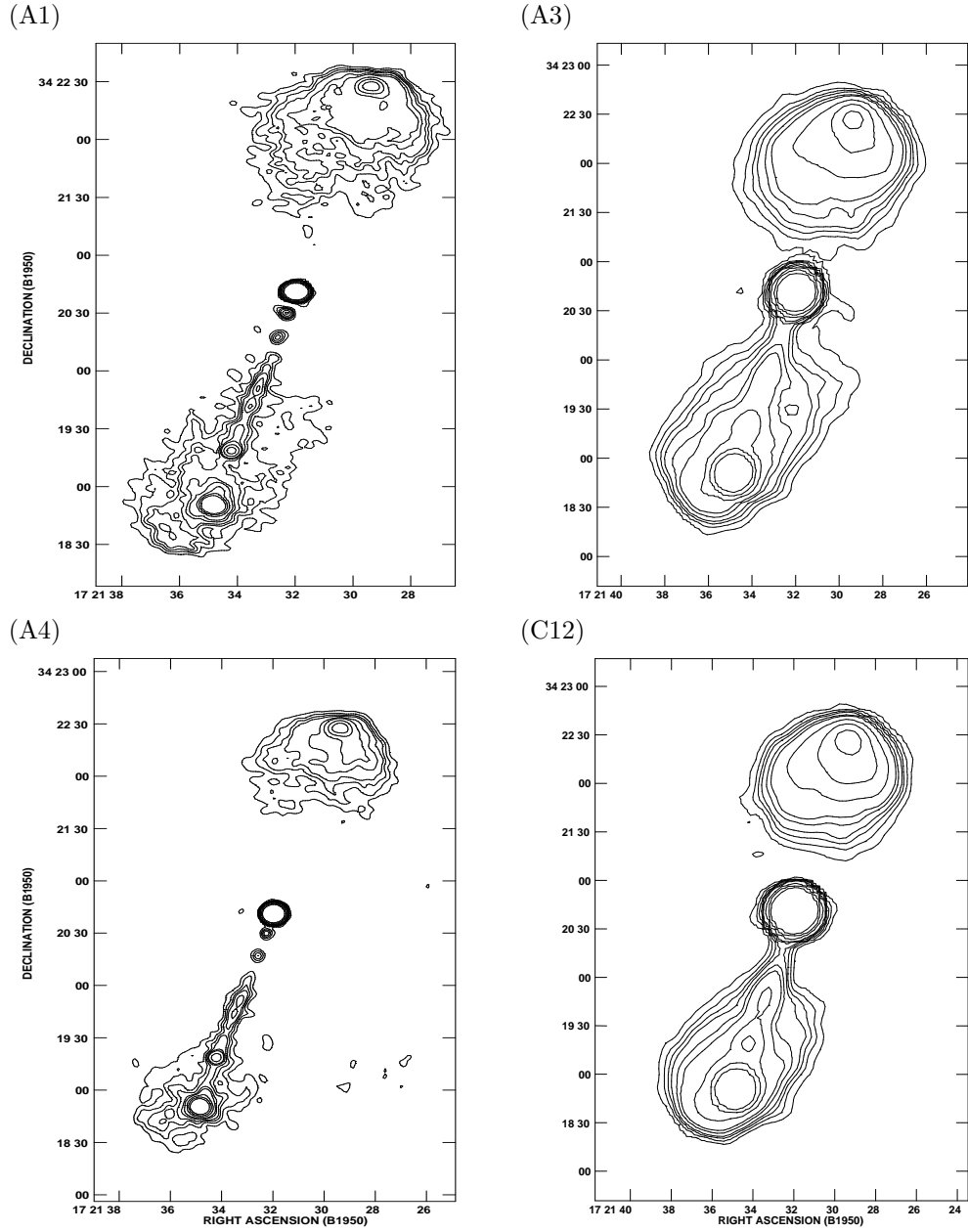


Figure 9: Contour plots of the four images. The contour levels are RMS (table (5)) times 3, 6, 9, 12, 18, 24, 48, 96, 192 mJy Beam^{-1} . The first contour represents 3σ detection. From top left to bottom right: High resolution 20cm image (A1), Low resolution 20cm image (A3), High resolution 6cm image (A4), Low resolution 6cm image (C12).

5.1 High Quality Multi-Resolution Combined Maps

5.1.1 Results of Combined Maps

Two maps with different resolutions and same frequency are combined together to get multi-resolution images. These show much more detail than any other image by itself. See figures (11) and (12) for the combined images A1+A3 and A4+C12 respectively. Some differences can be seen between the two combined images. The core is unresolved in both images and differ in strength. In the 1.4 GHz image the peak flux is higher than at the 5 GHz image, indicating a slowly decreasing spectrum $S_\nu \propto \nu^{-0.3}$. The core strength is measured at each observation and compared to earlier measurements with Westerbork Synthesis Radio Telescope (WSRT) done in 1973/74 [Conway et al., 1977] and with 1974/79 measurements [Jägers et al., 1982]. Evolution of the variable core can be seen in table (6). With this result, it is obvious that the core varies in time. Not only that but you can also see that the core seemingly loses power over the years. About $\sim 15\%$ decrease in 10 years at 1.4 GHz and $\sim 25\%$ decrease in 10 years at 5 GHz is showing. Because of limited measurements, this can easily be attributed to high variability of the unresolved core. The core is also proven to be highly variable at optical frequencies [McGimsey and Miller, 1978].

Very nice details of the jets are visible with these images. We can see at least four knots within the jet and one of the knots is extended over a larger area. No counter-jet is visible though. When looking at the diffuse structure, you notice that the image is much smoother at the shorter wavelengths. This implies the presence of small-scale structure at high frequencies.

The jets (including the invisible counter-jet) are remarkably straight: The core and hotspots are aligned to within 1° .

Table 6: Core strength comparisons.

Epoch	Flux density at 1.4 GHz	Flux density at 5.0 GHz	Observer
1973.9	580±20 mJy	—	Conway et al.
1974.3	—	508±20 mJy	Conway et al.
1976.9	610±30 mJy	—	Jägers et al.
1979.3	—	440±30 mJy	Jägers et al.
1984.1	480±6.6 mJy	—	Barthel et al.
1984.3	499±8.6 mJy	340±3.4 mJy	Barthel et al.
1984.6	—	339±5.5 mJy	Barthel et al.

5.1.2 Discussion of Combined Maps

Although, when comparing core intensity results with earlier researches it has shown a rapid decrease over the years, we must not forget that the previous results come from a different observing station with different resolution measurements. Moreover, the biggest difference is in the observed frequency. This is not exactly the same for all the measured points. Still, they should not differ all that much. We know that the core is highly variable, but there are too few data points to say that this kind of a fast decrease in core strength is a certainty.

The core is also observed and resolved with the VLBI in 1986/1988 [Hooimeyer et al., 1992]. They showed components moving away from the central spot, at superluminal velocities, which shows the arising of the jet and completely explains the variability of the core.

A rather remarkable comparison is made when comparing the knots in the jet of 4C34.47 to the knots in 3C47 made by Fernini et al. [1991], see figure (10). The morphology of the jet and the knots show striking similarity. There are three to four prominent knots within the approaching jet, with the second knot a bit elongated relative to the others. It raises the question that if these knots are always created the same way or is it just coincidence. It is quite possible that the nuclei of such objects have active and less active periods whereby these are directly visible in the jets like fingerprints of the activity and perhaps these activity periods are the same for all superluminal Quasars.

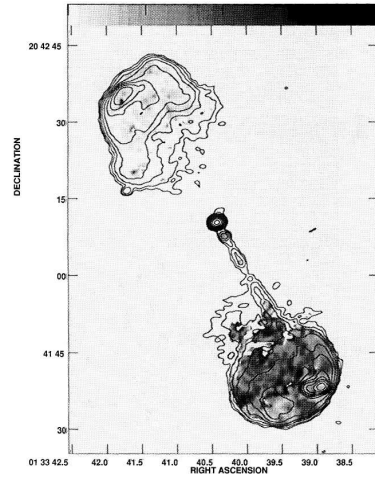


Figure 10: Radio contours of 6 cm total intensity map of 3C 47 plotted over a greyscale of the depolarization ratio made by Fernini et al. [1991].

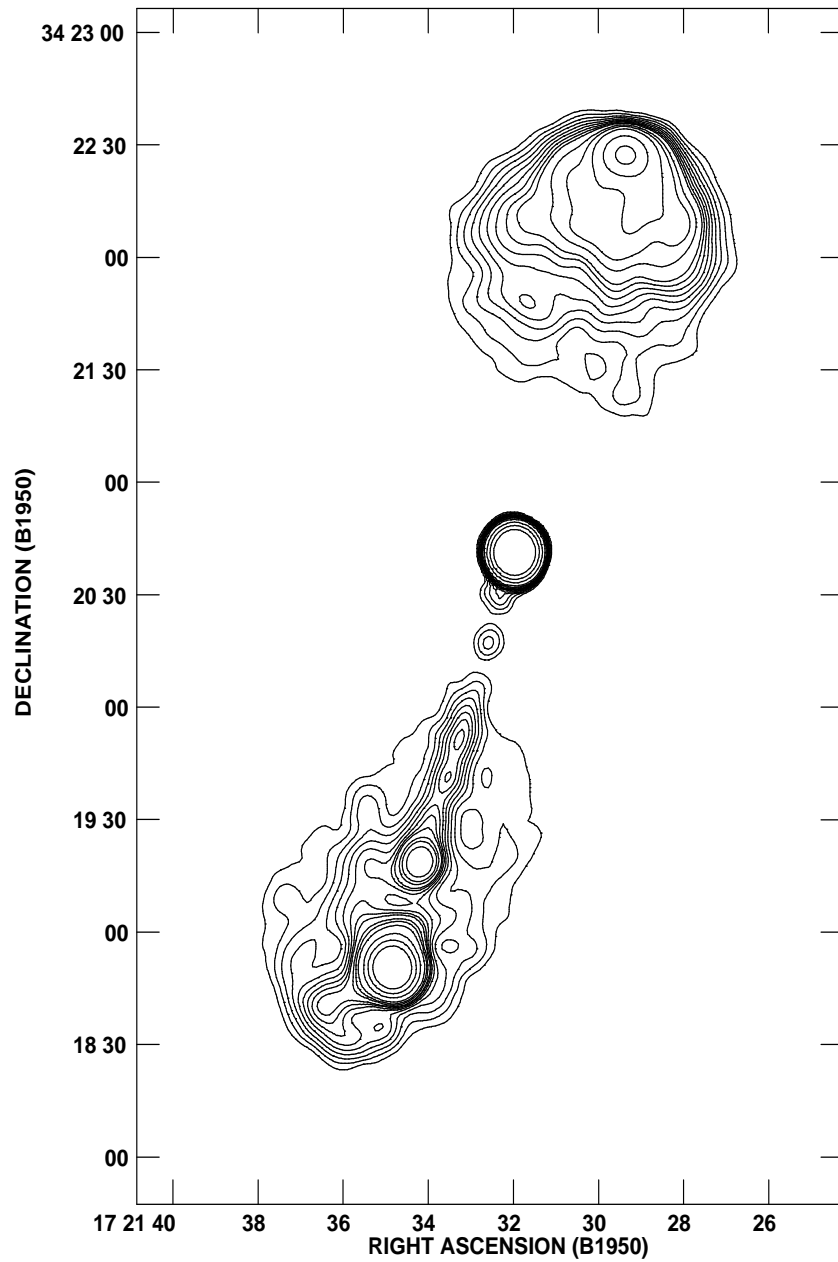


Figure 11: Combined 1.4 GHz image of two different resolution maps, A1 (see figure (9a)) and A3 (see figure (9b)). The FWHM of the clean beam is 7.5 x 7.5 in arcseconds. Contour levels are $0.25 * 4, 6, 8, 10, 12, 14, 16, 18, 20, 25, 30, 40, 80, 160, 320$ mJy/Beam.

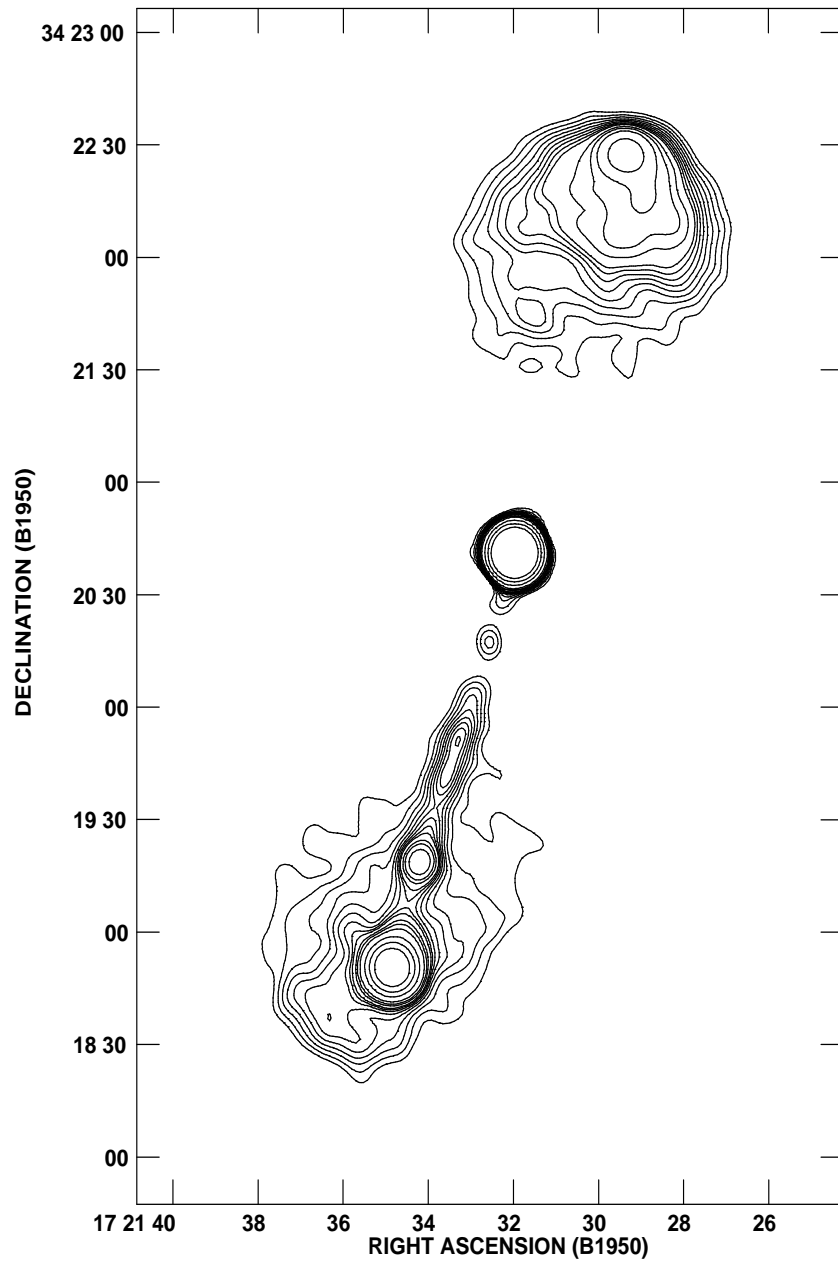


Figure 12: Combined 5 GHz image of two different resolution maps, A4 (see figure (9c)) and C12 (see figure (9d)). The FWHM of the clean beam is 7.5×7.5 in arcseconds. Contour levels are $0.109 \times 4, 6, 8, 10, 12, 14, 16, 18, 20, 25, 30, 40, 80, 160, 320$ mJy/Beam.

5.2 Spectral Index of 4C34.47

5.2.1 Results of Spectral Index

Between 1,4 GHz and 5 GHz an intensity comparison is made to find the spectral index α . This spectral index is attained because the frequency dependence of flux can be approximated with a power law function $S_\nu \propto \nu^\alpha$, where S_ν is the integrated flux density and ν is frequency. For a blackbody at the long wavelength side (Rayleigh-Jeans limit), $\alpha=2$, and for an ensemble of opaque synchrotron gas clouds, $\alpha=0$. Expected is to get an index diminishing towards higher frequencies where this drop should be steeper at the lobes and hot spots and flatter within the core. This has to do with the ageing of the electrons.

Spectral indices at several locations of the Quasar are measured. Covered locations are presented in figure (13). At both the hot spots (positions A and I), the index is quite steep, ~-0.86 and ~-0.88 respectively. This is very well within expectations. The lobes also show similar steep spectral indices ~-0.77 and ~-0.84 (B and H). The core has the flattest spectral index of ~-0.29 (C) and the only visible, southern, jet has an α range between -0.42 to -0.79 (D to G) measured at the knots. We estimate the spectral index error to be ± 0.05 . You can see all the values listed in table (7). Spectral index distribution of this Quasar is obtained using the $3.9''$ resolution maps.

Table 7: Spectral indices at different locations.

Position	A	B	C	D	E	F	G	H	I
Index α	-0.86	-0.77	-0.29	-0.75	-0.50	-0.42	-0.79	-0.84	-0.88

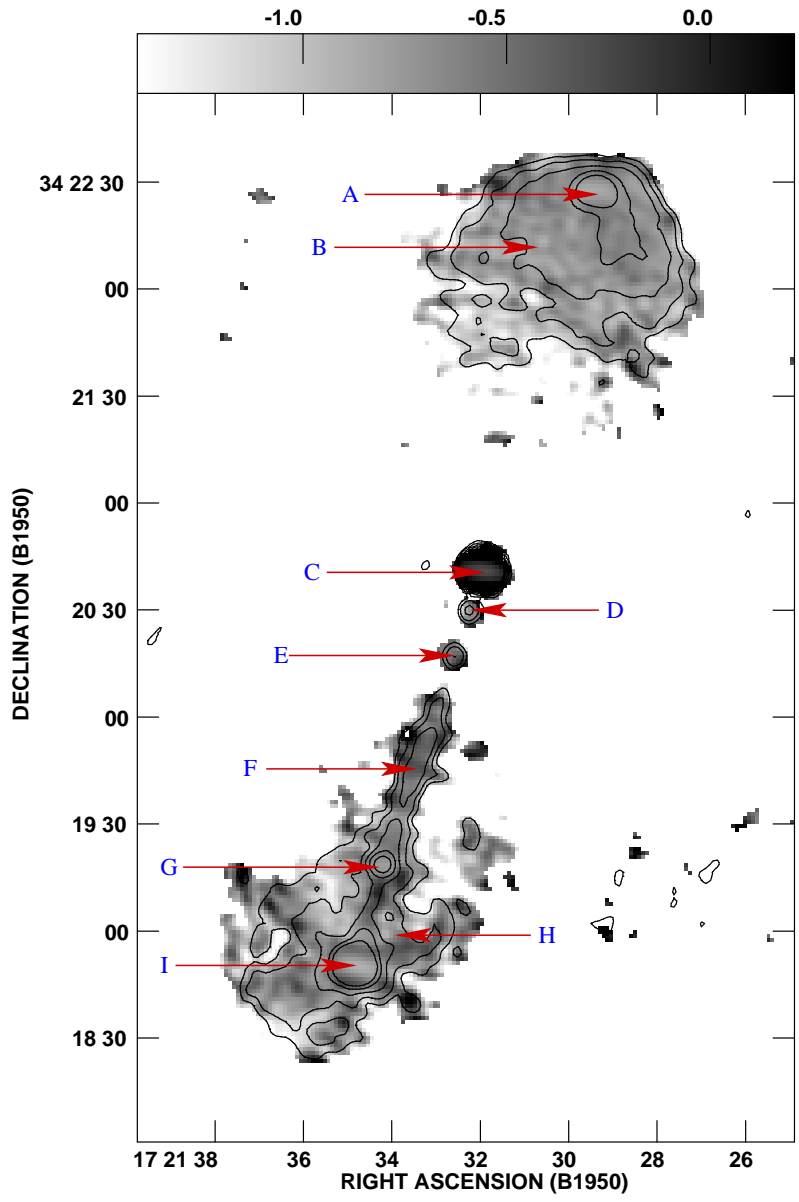


Figure 13: Gray scale representation of the spectral index between 1.4 GHz and 5 GHz with superimposed contours of total intensity.

5.2.2 Discussion of Spectral Index

Spectral index values of the components around the hot spots are very cluttered. They consist of a very broad range of indices. Considering this, the spectral index of these lobes are measured as an average over a small area around indicated positions. The lobes should have steep spectra, i.e. a strong declining slope α , as steep as the hot spots if not steeper, but this is not observed. However, where the lobes start or end is not very well defined. Furthermore, they span a great area where the energy distribution is not uniform and random processes affect the outcome of the results. This is the reason why averaging is the best way for determining α . As for the core, the exact center should have a complete flat spectral index, i.e. $\alpha=0$. The reason for this not being so is that for these resolution images, the core is unresolved. Using VLBI, the core was resolved and showed four components, where the true nucleus had indeed $\alpha=0$ and the other components are jet knots which are observed to be moving [Hooimeyer et al., 1992].

When comparing the measured spectral index values with the values obtained by Jägers et al. [1982], which are ~-0.75 at the hot spots and ~-0.25 in the center, we see that they are in agreement. Only slight differences exist which can be explained by their longer spectral range (0.6 GHz to 5 GHz) from which they obtain α and according to them the spectral index is flatter between 0.6 GHz and 1.4 GHz for the core.

5.3 Polarization of 4C34.47

5.3.1 Results of Foreground Rotation & Rotation Measure

Polarization properties are examined by looking at the polarization intensity, degree of linear polarization and polarization angle maps of the Quasar. These are obtained by combining I, Q and U maps of the data as formulated in equations (2) through (4), in the same order as mentioned above.

$$P = C \cdot \sqrt{Q^2 + U^2} \tag{2}$$

$$\Pi_L = \frac{P}{I} \tag{3}$$

$$\varphi = \frac{1}{2} \tan^{-1} \frac{U}{Q}, \tag{4}$$

where the factor C is a noise-based correction for Ricean bias.

In figures (14), (15) and (16) all of the combined P and φ images and Π_L and φ images superposed on total intensity maps are shown.

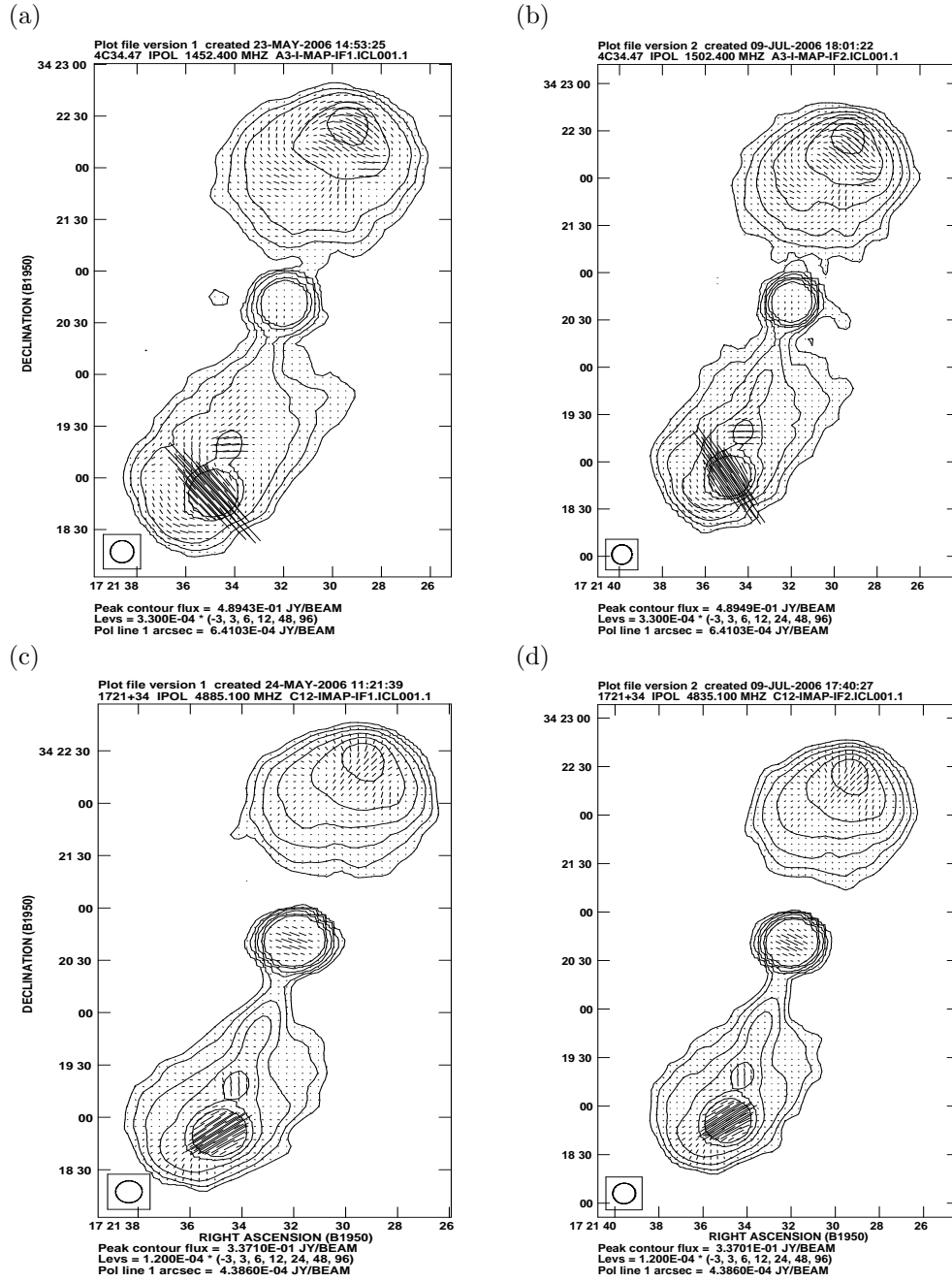


Figure 14: Contour map of the total intensity with polarization intensity and E-vectors overlaid at different frequencies. (a) 1452.4 MHz (b) 1502.4 MHz (c) 4885.1 MHz (d) 4835.1 MHz.

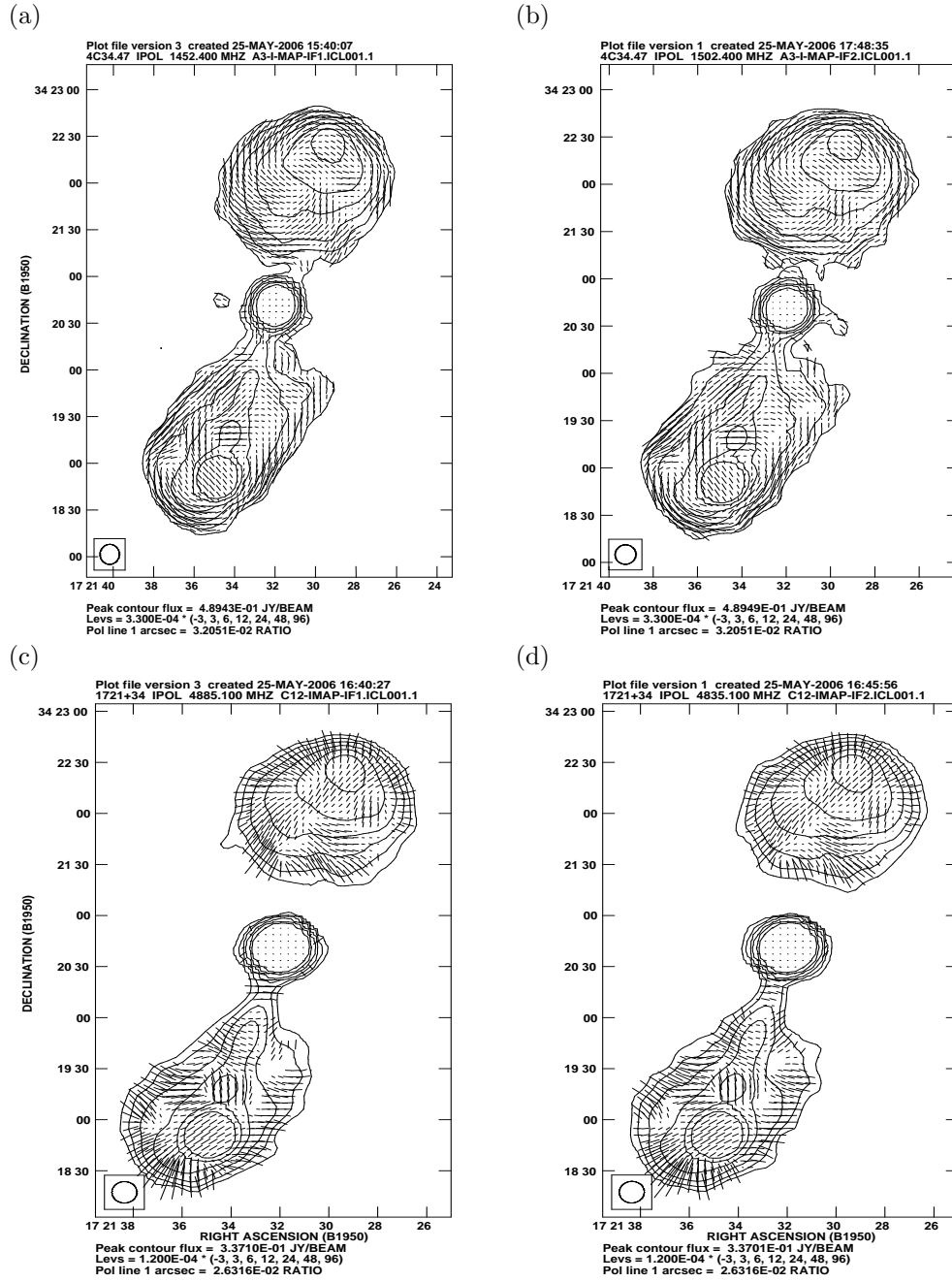


Figure 15: Contour map of the total intensity with linear polarization degree and E-vectors overlaid at different frequencies. (a) 1452.4 MHz (b) 1502.4 MHz (c) 4885.1 MHz (d) 4835.1 MHz.

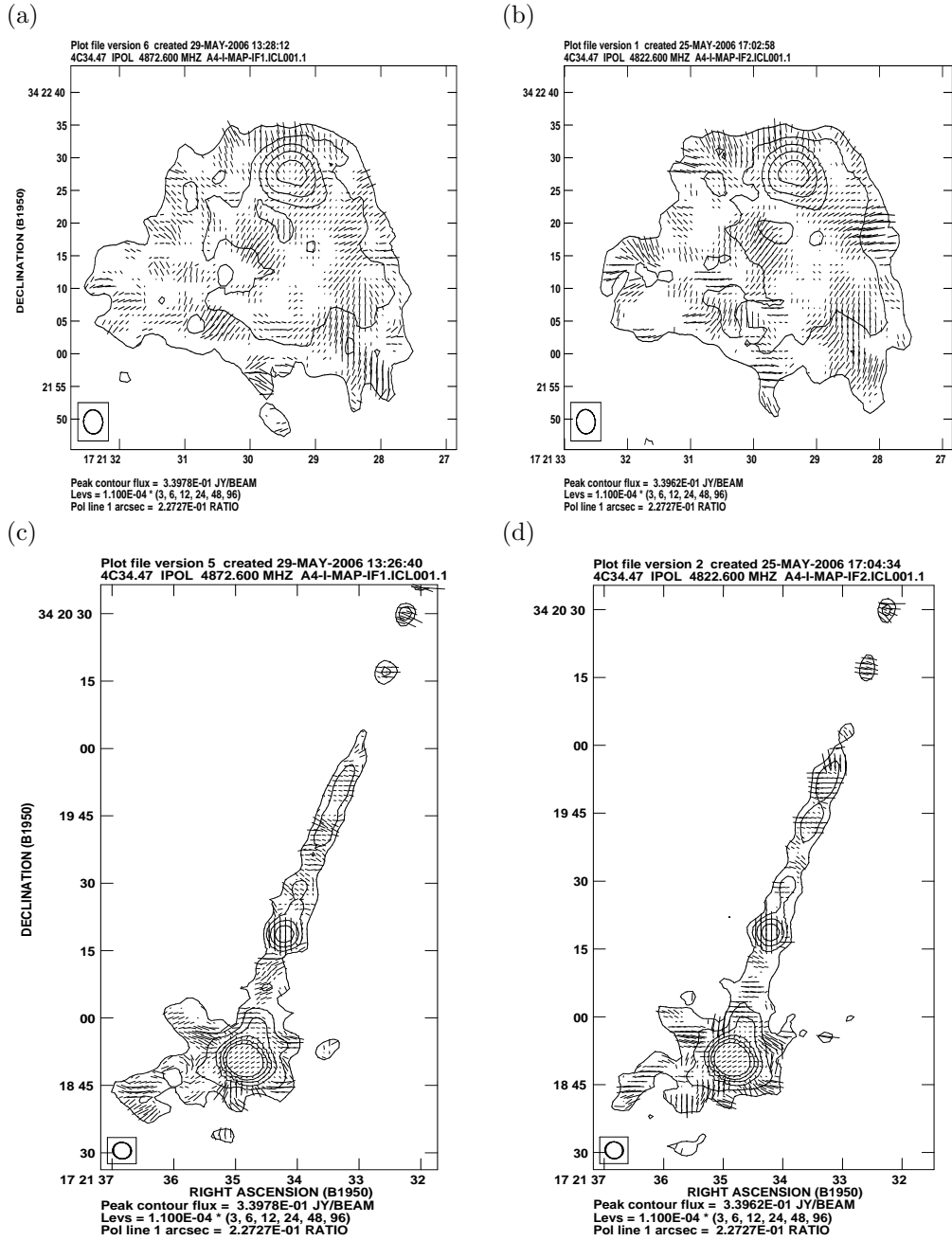


Figure 16: Total intensity contour maps of north and south side of both IFs of A4, with linear polarization degree and E-vectors overlaid. (a) North lobe at 4872.6 MHz (b) North lobe at 4822.6 MHz (c) South jet + lobe at 4872.6 MHz (d) South jet + lobe at 4822.6 MHz.

In these images, the lines indicate the direction and strength of the electric field. Each map is plotted with both IFs separately. In figure (14), the polarization intensities of the two 14 arcsecond observations are plotted together with their polarization angles. Reason for showing $\sim 14''$ resolution images is that here the polarization is much better viewed than at high resolution plots. The polarization strength in here is in absolute values. This results in a high polarization intensity which is seen in the southern hot spot, as this area is not only highly polarized, but also highly intensified as a result of beaming. Difference with the core or the northern hot spot is, either it is more intense but much less polarized (core) or vice versa (northern hot spot). To compensate for intensity, Π_L , the ratio of polarization intensity against total intensity is plotted, see figures (15) and (16). From these second set of images (figure 15), it is clear that the lobes around the hot spots display the most polarized radiation. As we look at the direction of the electric field lines we immediately see the change between the 1.4 GHz and 5 GHz plots and this rotation of the field lines between the two frequencies is due to the Faraday effect. Magnetic field lines in the line of sight parallel to the direction of propagation are the cause of this Faraday effect. The amount of rotation is in the order of $\sim \frac{1}{2}\pi$ radians or $\sim 90^\circ$. With only two frequencies, the rotation can also be $n\pi$ ambiguous, that is $\frac{1}{2}\pi \pm n\pi$. Best way to determine Faraday rotation is to have at least three different observing frequencies. This could not be achieved properly with only two frequencies. An ingenious idea suggested and adopted was to split up the two IFs of each map and to plot them separately. If there is no ambiguity, the rotation between the intermediate frequency maps, which is 50 MHz frequency difference, should be small. As the absolute difference of λ^2 between the two IFs of 20 cm observation is bigger relative to 6 cm, more rotation is expected to be seen at longer wavelengths. To test this expectation, a strong polarized area (southern hot spot) is zoomed in, figures (17) to (20), and the rotation measured at this position is $\sim 6^\circ$ for the 20 cm map. For 6 cm map, the rotation is found to be $\leq 1^\circ$, which proves that there is no $n\pi$ ambiguity.

The precise rotation measure (RM) of the Quasar is found with three frequencies, i.e. 1452.4 MHz, 1502.4 MHz and 4885.1 MHz, using;

$$\beta = RM \cdot (\lambda_2^2 - \lambda_1^2), \quad (5)$$

where β is the measured angle of rotation.

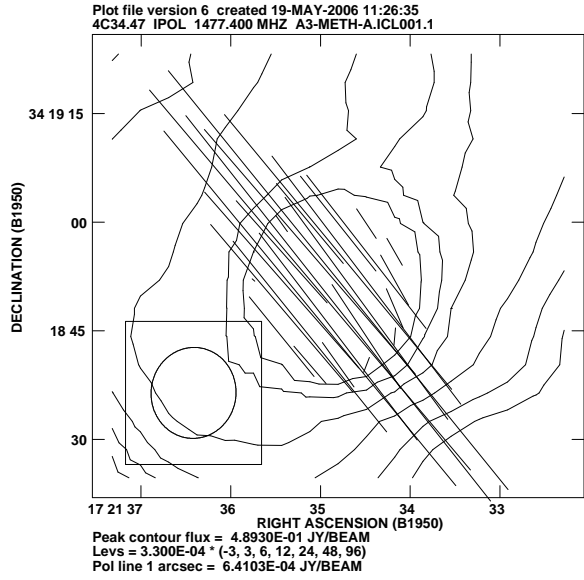


Figure 17: Polarization intensity and angle plotted over a contour map of the southern hot spot of observation A3. Intermediate frequency at 1.4524 GHz.

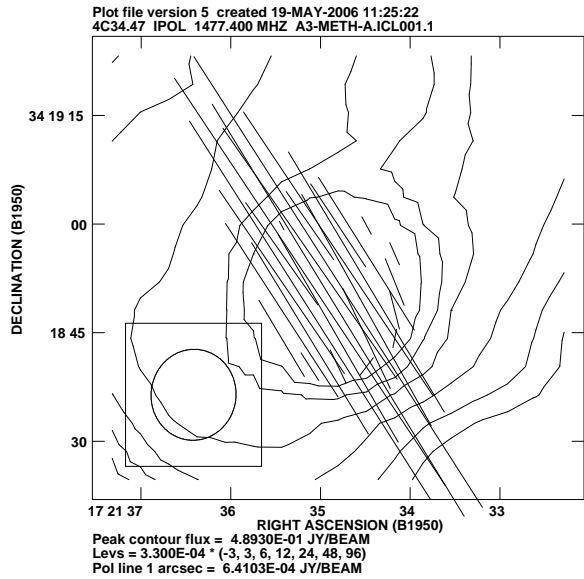


Figure 18: Polarization intensity and angle plotted over a contour map of the southern hot spot of observation A3. Intermediate frequency at 1.5024 GHz. Note the small rotation with respect to the other 20 cm IF (figure 17).

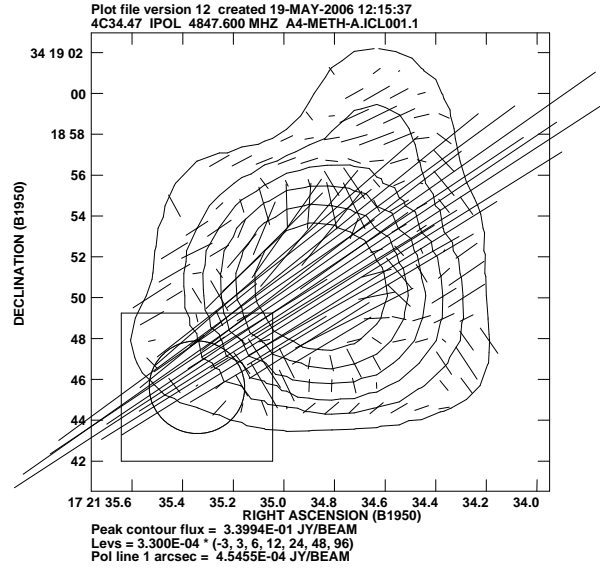


Figure 19: Polarization intensity and angle plotted over a contour map of the southern hot spot of observation A4. Intermediate frequency at 4.8726 GHz.

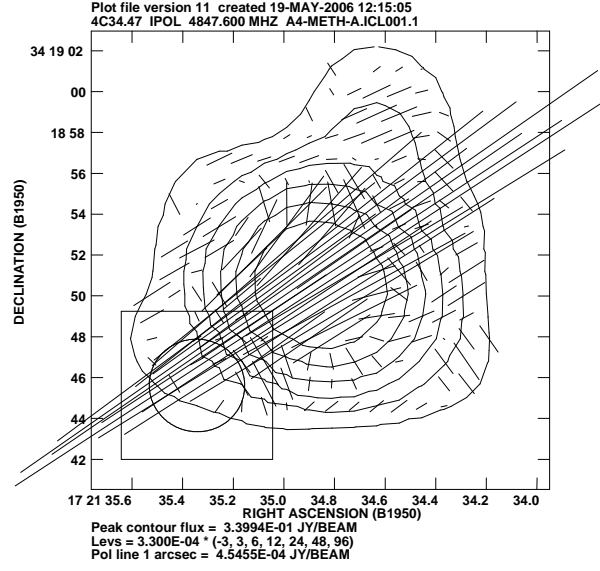


Figure 20: Polarization intensity and angle plotted over a contour map of the southern hot spot of observation A4. Intermediate frequency at 4.8226 GHz. The 6 cm rotation difference is substantially smaller than at 20 cm.

At some of the locations as pointed in figure (13), the RM values are measured and put into table (8). The integrated Faraday rotation measure for 4C34.47 is 41.4 rad m^{-2} . This translates to a Faraday rotation of 92.13° .

Table 8: RM values at specific locations.

Position	RM (rad m^{-2})	σ_{RM} (rad m^{-2})	Rotation β ($^\circ$)	σ_β ($^\circ$)
A	44.51	6.45	99.05	14.35
B	36.88	4.25	82.07	9.46
C	41.60	3.17	92.57	7.05
H	42.47	10.14	94.51	22.57
I	37.75	4.96	84.01	11.04

5.3.2 Discussion of Foreground Rotation & Rotation Measure

Until now only linear polarization is considered. There should not be any circular polarization within the radio waves of such sources. To see if this is true, the Stokes V parameter is plotted in a histogram in figure (21). The Gaussian shape centered around 0 Jy shows that there is no circular polarization present. Both the whole source and of the noise show the same histogram shape. This is also good to see if there are any systematic errors done in calibration.

Rotation of electric and magnetic vectors of linear polarized radiation from Quasar 4C34.47 is mainly due to our own Galaxy. That the integrated rotation turned out to be pretty close to 90 degrees is just a coincidence and not some change from electric to magnetic fieldlines, which are also perpendicular. However, the rotation is not entirely uniform throughout the whole source. As seen in table (8), it ranges generally between 80° to 100° . If intrinsic, there may be considerable amount of thermal material within the radio lobes. In 1987, Leahy conducted a study on the amount of variations to RM by galactic Faraday rotation. According to his study, RM variations for sources within 10° of the galactic plane is $\approx 20 \text{ rad m}^{-2}$ and 6 rad m^{-2} for sources near the galactic pole. The galactic latitude of 4C34.47 is 32.18° . As the maximum RM differences across this extended Quasar is around 9 rad m^{-2} (see table (8)), the whole dispersion can be explained by our own galactic foreground, because the fluctuations can occur on scale sizes at least as small as 20 arcseconds [Leahy, 1987]. This also explains the large error values to the rotation. Another plausible solution is that this might be of extragalactic origin. Except that there are no known large polarization rotators in the foreground of this object.

5.3.3 Results of Depolarization Asymmetry

If the Faraday rotating medium is located between the source and the observer, then the only effect is a net rotation of the plane of polarization, but if the Faraday rotating medium is mixed up with the emitting region, then radiation

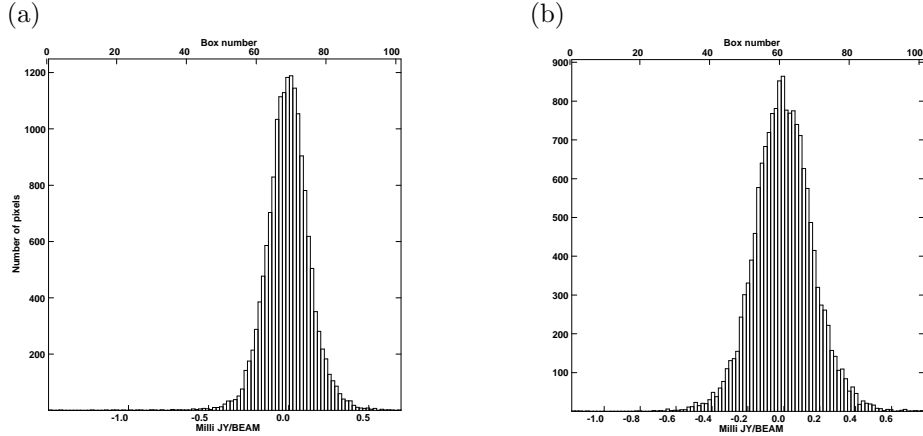


Figure 21: Histogram plots of circular polarization of 4C34.47. Plot (a) shows the V-polarization of 1452.4 MHz image and (b) of the 4885.1 MHz image.

emitted from different depths along the line of sight are rotated by different amounts, thus reducing the net polarization.

This Faraday depolarization is measured at twelve different areas of the Quasar. Eight of the selected locations are chosen to be large areas, because larger areas will give more averaging over the polarization intensities thus the result will be more accurate. These eight locations are selected by dividing the north and the south lobe each into four equally sized pieces. Three of other the four locations are at the brightest spots, the core and the two hot spots. The last location is at the very south end of the north lobe, where the counter-jet ends. This is the closest location to the core on the north side with still good detection. The DP is the depolarization ratio between P/I (at 6 cm) and P/I (at 20 cm). This means that higher DP values stand for more depolarization. Values significantly smaller than unity suggests re-polarization. We would expect to find much more depolarization at the northern locations of the quasar than at the southern locations as explained in section 1.3.2 with the use of figure (6). With a few exceptions which will be discussed later, no depolarization is found at all. The measured locations and the DP values are listed in table (9). Except for the core and the one location closest to the core, all the values are within $DP = 0.92$ to 1.18 . This is far too small a value to say something about depolarization, or re-polarization for that matter. All these values are negligible for depolarization and it is safe to conclude that there is no depolarization asymmetry over the whole Quasar. This in itself is a remarkable result. There is however small significant depolarization seen in the bridge towards the Northern lobe and also does the core show some depolarization.

Table 9: DP values at different areas.

Lobe North of the Central Feature	Π_{6cm} (%)		Π_{20cm} (%)		DP	
	IF-1	IF-2	IF-1	IF-2	IF-1	IF-2
At the Hot spot	9.20	9.80	9.44	9.58	0.97	1.02
North-side Hot Spot Area	9.63	9.76	9.56	9.72	1.01	1.00
East-side In the Lobe	13.05	12.11	11.94	11.84	1.09	1.02
West-side In the Lobe	8.98	8.94	9.17	9.12	0.98	0.92
South-side Jet Area	11.06	10.06	9.37	9.51	1.18	1.06
Lobe South of the Central Feature	Π_{6cm} (%)		Π_{20cm} (%)		DP	
	IF-1	IF-2	IF-1	IF-2	IF-1	IF-2
At the Hot spot	12.56	12.57	12.84	12.90	0.98	0.97
South: Hot Spot Area	12.28	12.15	12.58	12.76	0.98	0.95
East: In the Lobe	15.74	15.24	16.44	16.56	0.96	0.92
West: In the Lobe	9.36	9.59	9.46	9.94	0.99	0.96
North: Jet Area	10.81	11.08	10.94	11.19	0.99	0.99
Around and At the Central Feature	Π_{6cm} (%)		Π_{20cm} (%)		DP	
	IF-1	IF-2	IF-1	IF-2	IF-1	IF-2
The core	0.91	1.00	0.20	0.23	4.48	4.29
Bridge towards the Northern lobe	14.07	14.77	10.77	11.46	1.31	1.29

A very similar one-sided jet quasar 3C 47 was observed by Fernini et al. [1990] with the VLA. The redshift of this quasar is 0.425 and the object has a linear size of 300 kpc. Fernini and his colleagues were able to measure a strong depolarization asymmetry. From their results they conclude that the B-field in the halo surrounding 3C 47 has a strength of 0.2 - 2.5 μG . The major difference between this Quasar and 4C34.47 is the size; 4C34.47 is 2.7 times larger in linear size, which may be the main cause for this difference.

5.3.4 Discussion of Depolarization Asymmetry

The results are unexpected but not incomprehensible. Because this is a very large source, the depolarizing medium may not encompass the whole source. This explains the absence of depolarization asymmetry at the lobes. Strengthened by the fact that there is some depolarization within the core and at the closest location to the core. It can be debated that the core has a very low degree of polarization and the measured DP may be exaggerated by the measurement errors. I believe this is not the case. Relative to the other locations, the core has a significant difference in polarization degree between the two wavelengths. This shows that there is more than only the relatively large measurement errors at the core. This non-asymmetry result is in concordance with Garrington et al. [1991] results for extended sources. They have compared 47 double radio sources with 22 of them being large (over $\sim 30''$ angular scale) and measure a significant asymmetry for the smaller ones but not for the large sources. I claim that there still can be measured DP asymmetry in large sources when searched close to the core, as the core measurement results here hint to that. The DP is very dependant on the size of the depolarizing halo. It must be possible to find high DP when looked at or close to the core in other extended objects where initially no significant asymmetry was discovered.

An interesting option is to find the size of the halo by looking at the DP asymmetry at various points along the length of the source. The only thing needed for this is a reasonably detectable counter-jet. By only looking at the approaching jet and searching for a significant change in depolarization, the size of the halo can in principle be measured, but to do this it is needed to have observations with at least three (favourable) frequencies at sufficient S/N and that is certainly not easy.

6 Depolarizing Medium

What causes depolarization? There are many possibilities which can be considered. Any magneto-ionic thermal plasma within the emitting regions will contribute to depolarization [Burn, 1966]. This does not explain why both lobes exert different depolarization ratios if they are indeed created in the same fashion. Furthermore, as Garrington et al. [1991] show, the medium responsible for the asymmetry is not likely to be ISM but rather the IGM because they find that the differences in RM between the lobes do not correlate with the Faraday dispersion factor, see equation (6).

$$\sigma^2 = n_e^2 B^2 d$$

$$\Delta^2(x) = \int_{\infty}^x \sigma^2 dl \quad (6)$$

From X-ray observations, a presence of a halo of hot gas has been revealed around many galaxies and this is most likely the dominant factor causing depolarization. With the halo gas depolarizing model, DP asymmetry is easily explained by the orientation of the source. This also goes very well with the orientation related explanations for beaming, jet-sidedness and unification. As explained before, asymmetry originates from the difference in path lengths between two points of the source. Assuming a spherical shape of the depolarizing medium and assuming an electron density n_e and magnetic field strength B both to be uniform in a minimum path length d_{min} , the DP asymmetry exists if the source is inclined at an angle θ towards the line of sight. Anything outside the source will not prefer one spot over the other, unless that medium has a very extraordinary shape or is positioned in such a way that it only covers one area of the source. The latter possibility is actually not unimaginable, especially for extended sources, but will not be considered here.

Next to the orientation of the object, the size of this halo of hot gas relative to the source size determines how big the difference is in depolarization. Biggest asymmetry should occur at the edges of the source, where the path length difference is the greatest. For the cases where the deprojected source size is larger than $D / \sin(\theta)$, where D is the diameter of the halo, parts of the source will not be depolarized by the halo. This must be the case for extended sources and the solution to why they are not showing any or as much depolarization compared to the smaller sources as the results of Garrington and Conway [1991] are showing. This idea is strengthened by the fact that there are high degrees of polarizations measured for many Quasars and RGs, which would not have been possible if the halo size was extremely large, in effect depolarizing more. Therefore, the maximum halo size for measurable depolarization asymmetry cannot be larger than roughly 10 times the source size. In fact, Garrington & Conway argue that the source size should equal roughly the halo diameter. For the better part of their sample of Quasars which have a median projected source size

of about 150 kpc, they conclude that the typical halo core radius must be about 100 kpc (assuming $\theta = 45^\circ$). If the halo model is correct for the depolarization of radio sources, then this is the best and the most logical explanation for the DP symmetry of 4C34.47.

There has been some critique to this orientation model. Depolarization studies like the one by Fernini [2001] could not find convincing differences of DP ratio's between RGs and Quasars. Liu and Pooley [1991a,b] found a correlation between spectral index and amount of depolarization in their sample of powerful Radio Galaxies. They suggest that the origin might be due to non-symmetrical emission line gas around the host galaxy, which are usually found in high z and powerful sources. Such a correlation should not depend on the angle but rather on environmental or intrinsic effects. Though, there is a big difference between the researched samples of Liu & Pooley and Laing & Garrington, as the sample by Liu-Pooley consists of much more powerful sources ($\gtrsim 10^{27}$ W/Hz) at high redshift and consists chiefly of Radio Galaxies and the sample by Laing-Garrington consists chiefly of Quasars.² Dennett-Thorpe et al. [1999, 1997] investigated correlations between spectral index, jet side and extend of the radio lobes and they found that the sample differences were mainly due to redshift rather than orientation as did Goodlet and Kaiser [2005]. These studies pose problems for the viewing angle explanation. Though, there is a lot of proof that there are other effects that play a significant role, none of them can completely set aside the orientation related effect of the depolarization by the halo. A good remark by Fernini was that the environments around these sources may wash out the orientation effect. Perhaps even the medium between the source and the observer can wash out some of the orientation effect. This would certainly explain the redshift dependence as well as the spectral index correlation. In any case, the Laing-Garrington effect explanation still can survive all this critique.

²An interesting side note is that in the early nineties, this heated issue was much debated back and forth by the two sides. To this date, it is still not resolved.

7 Properties of the Radio Jet

By measuring the jet-counter-jet flux density ratio and knowing the bulk flow velocity of the jet, the angle that the object makes to the line of sight can be recovered very easily assuming that the Doppler boosting is the main cause for the asymmetrical appearance. This can be estimated using equation (7) [Scheuer and Readhead, 1979].

$$\frac{S_j}{S_{cj}} = \left[\frac{1 + \beta_j \cos\theta}{1 - \beta_j \cos\theta} \right]^{2-\alpha}, \quad (7)$$

where β_j is the velocity of the jet in units of c and α the spectral index of the jet. If on the other hand the angle is known but the velocity needs to be recovered, equation (7) can be rewritten in the form for β , see equation (8). Equation (9) gives the corresponding Lorentz factor.

$$\beta_j = \frac{1}{\cos\theta} \cdot \frac{s-1}{s+1} \quad (8)$$

$$\gamma = 1 / \left\{ 1 - (1/\cos^2\theta)[(s-1)/(s+1)]^2 \right\}^{\frac{1}{2}}, \quad (9)$$

where $s = (S_j/S_{cj})^{\frac{1}{2-\alpha}}$.

The average spectral index of the jet obtained from the results in table (7) is -0.62. As for the jet-counter-jet ratio, because there is no detectable counterjet, a lower limit is measured at $S_j/S_{cj}=24.0$ with a sigma of 2.9. Using the highest possible jet speed c , knowing of course this can never be achieved, and by rewriting equation (8) and filling in the numbers in equation (10), results in an upper limit to the angle θ of 57° .

$$\theta = \arccos \left(\frac{1}{\beta_j} \cdot \frac{s-1}{s+1} \right) \quad (10)$$

This means that with a very high certainty that the angle to the line of sight of Quasar 4C34.47 can not be any larger than 57° . The actual speed of the jet must be smaller than the speed of light. Besides, the flux density of the approaching jet is taken as an average over the whole jet and since the counter-jet is not detected at all, the maximum flux at any point on the approaching jet could also have been used to get the ratio. This would have resulted in a much higher lower limit to flux ratio. The dependence of the velocity to the angle at this flux ratio is presented in figure (22). For reasonably relativistic speeds ($\geq 0.9c$), this implies that for the measured ratio, the range of the angle is 4° between 53° to 57° .

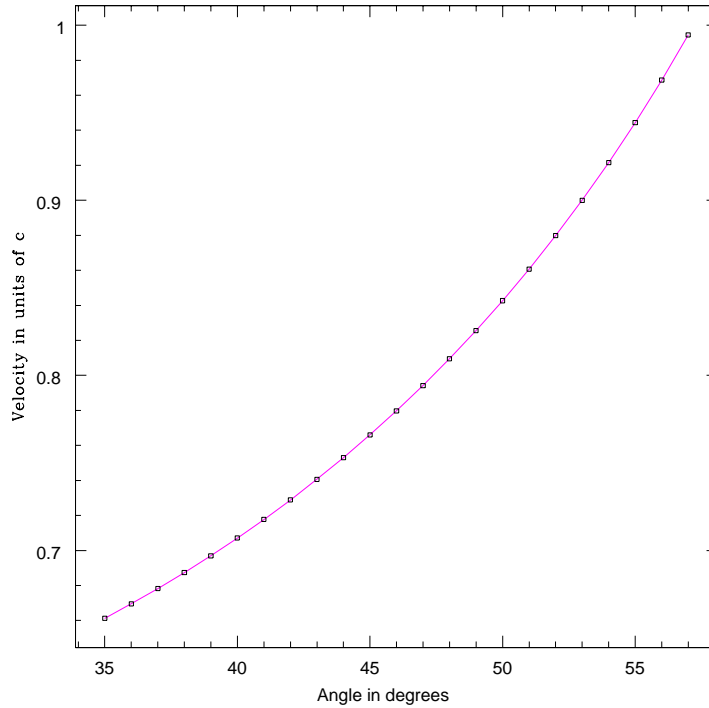


Figure 22: Dependence of the jet velocity to the angle at a flux ratio of $S_j/S_{cj}=24$

Barthel et al. suggested in 1989 that 4C34.47 lies within 44° of the line of sight with a minimal possible angle of 22° after their measurements of the apparent superluminal velocity. They had found apparent velocities of the @two knots closest to the core of the approaching jet to be $\beta = 1.9 \pm 0.7$ and $\beta = 3.4 \pm 0.4$. The 44° limit finds its origin in the general unification model for extragalactic radio sources, whereby Quasars are oriented within a 44° cone. This would suggest a flux ratio of more than twice the measured ratio. In figure (23) the flux ratio versus the angle to the line of sight is plotted with the velocity fixed at $0.9c$.

This conclusion to such a low upper limit to the angle shows that we look at this Quasar at a small angle and the deprojected size is at least $817\text{kpc} / \sin(57^\circ) = 972\text{ kpc}$ and very possibly at an angle smaller than 44° , with the deprojected size is larger than 1.18 Mpc . Knowing now that there are many more large and even much larger sources out there, this Quasar does not become "uncomfortably" large at these sizes. The outcome fits well into the relativistic beaming model.

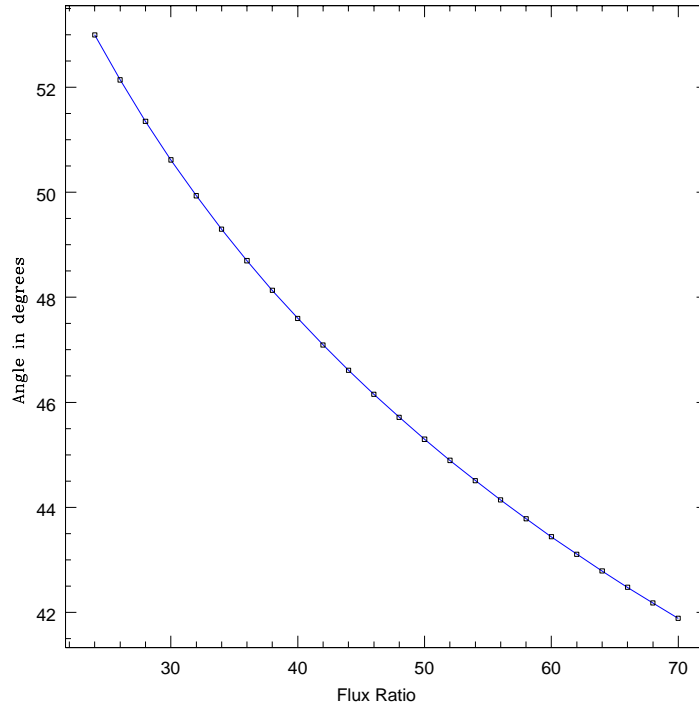


Figure 23: Dependence of the flux ratio of S_j/S_{cj} versus the angle at a relativistic speed of $0.9c$

From high resolution polarization images, see figure (16), the details of the magnetic-field lines can be seen. Most of the magnetic-field lines follow nicely the direction of propagation of the jet, except within the last knot. Here, the field lines are almost exactly in an opposite direction. How this came to be is quite a mystery. Unfortunately, there aren't many detailed polarization studies of Quasar jets to compare this result with. We can only theorize about it at this moment. There can be three explanations for this.

- (1) This may be due to a shockwave which distorts the surroundings and is intrinsic in nature.
- (2) There may something be within the path of the jet causing such a radical change in field lines.
- (3) The backflow of the lobe connects here and causes such an effect.

To say something about (1) is difficult, but about (2) and (3) opinions can be made. Starting with the second possibility, it must be said that this really

sounds unlikely. If there was something within the path of the jet, for a large object, the jet could have easily been diverted under an angle. However, the straightness of the jet is not broken. Furthermore, the approximate equal length of core-lobe and core-counter-lobe could have easily been compromised. For a small object within the path of the jet, the field line change seems too radical. The third mentioned possibility sounds very reasonable, as the magnetic lines within the lobe show similar large rotations. Additionally, the steep spectral index at this knot indicates that there probably is a lot of mixing of aged electrons. Coming back to (1), shocks can happen when fast moving particles catch up with slower or come in contact with piled up particles. A smooth pressure gradient builds up until it is so high that a shock occurs. In jets, shocks happen due to sudden changes in speed causing one body of gas to move into another. This might be brought about by variation in pressure of the surrounding medium or by variations in the speed at which material is injected into the jet. Either case can not explain the change of magnetic-field lines in only one of the knots very well.

The jets themselves are confined into a tight area, collimated by the hydro-magnetic disk winds [Blandford, 2000]. The powerful collimation and the high flow velocities give the jet a fine thin structure.

8 Concluding Summary

I have made detailed dual-frequency multi-resolution images of the double-lobed Quasar known as 4C34.47. The images I made are from the data taken with the VLA in 1984 at 1.4 GHz and 5 GHz. Until now, the data were never fully analysed and from that date never again is this Quasar observed at radio frequencies. These images show the structure and morphology of 4C34.47 as never have been presented before. The multi-resolution images show the detailed structure of the jets as well as the diffuse structure of the lobes around the two hot spots. Upon further analysis, this Quasar has shown a very strong core, quite unusual for lobe dominated sources. This core also shows a high variability and perhaps decreases in strength. I have compared all of the results to another study of 4C34.47 by Jägers and colleagues in 1982.

The obtained spectral index α at the lobes, measured between 1.4 and 5 GHz, are equally steep at both ends and shows no dependence to the side, with $\alpha=-0.86$ and $\alpha=-0.88$ at the North and South side respectively. The core shows a relatively flat spectral energy distribution and the jet is between $\alpha=-0.42$ and -0.79 . The spectral index results are in good agreement with what Jägers et al. had found. This result does not agree or disagree with the Liu-Pooley effect, which is the correlation between spectral index and the depolarization found by [Liu and Pooley, 1991a]. Nor is it in contrast with it, as there also is no depolarization asymmetry detected in 4C34.47. In their second paper, Liu & Pooley (paper b) discuss the presence of an non-symmetrical distributed emission-line gas around the host galaxy and suggest that this could account for the observed asymmetries. Keeping this in mind, I also have looked for the predicted depolarization asymmetry for preferably oriented radio sources, the Laing-Garrington effect, and that too was not detected in 4C34.47, except possible in its inner part. For both these cases, the earlier suggested solution might account for them. The size of this source may just be too great that the lobes fall outside of the halo and the emission-line gas around the host galaxy. To be sure of this, many more giant Quasars should be tested for depolarization and spectral index asymmetry.

The symmetrical findings do not offer proof for the beaming model, but the jet sidedness and the jet-counter-jet flux ratio is unaffected by size of the source and does imply that 4C34.47 makes a large angle to the plane of the sky. I have measured the angle to be maximally 57° to the line of sight and more likely to be smaller than 44° with an interpolated flux ratio between the two jets of 56:1. I have concluded that the issue of jet-sidedness finds a good explanation in relativistic flow, whereby the approaching jet is boosted in strength and the receding jet weakened resulting into this phenomena.

Another important issue is that rotation measure is sometimes connected to depolarization and that high RM means that there also is much depolarization. What I have measured is 92.13° RM throughout the source. Since no depolarization is detected, this could mean that they are not correlated or there simply is little or no material to depolarize the radiation. This, together with the depolarization measured at the core support the source size versus halo size

theory. The RM itself originates most likely by our own galactic foreground. The measured amount of rotation is 41.4 rad m^2 . Though small scale variations are quite large, in the order of $\sim 9 \text{ rad m}^2$, they still can be completely attributed to our galaxy. RM variations 6 up to 20 rad m^2 from the Galactic pole to 10° within the Galactic plane can be appointed to this foreground and variations can occur even at very small scales (20 arcseconds).

In the end, it can be easily said that there are still many issues that can be debated, but investigating other extended and oriented Quasars to see if there can be found similarities with 4C34.47 will contribute greatly to given explanations.

Acknowledgements

Getting to the end and finishing the thesis was a big task and I would like to thank all those people who helped me along the way.

First of all, I would like to thank my supervisor Peter Barthel for being there whenever I needed help and guidance. I have learned many things from him, especially how he finds it so important that you enjoy your work above all and that, I will never forget.

I would also like to thank all the staff members of the institute for their help especially Marco Spaans, his door was open for me whenever I needed him, Greta de Vries, Marc Verheyen, Wim Brouw, Bob Sanders, Ger de Bruijn, Wim Zwitter and Eite Tiesinga.

I am also indebted to my good friends Umut Yildiz, who read my thesis and helped me with correcting my mistakes and gave me good tips with a lot of other things and Derek Land, who has a great way with computers.

Finally, I would like to give special thanks to Robert Laing and Richard Strom, who came to the institute to look at my research and helped pushing me into the right direction.

References

- R. R. J. Antonucci and R. Barvainis. The cores of lobe-dominant quasars. *ApJ*, 325:L21–L23, February 1988.
- P. D. Barthel. Is every quasar beamed? *ApJ*, 336:606–611, January 1989.
- P. D. Barthel, J. R. Hooimeyer, R. T. Schilizzi, G. K. Miley, and E. Preuss. Superluminal motion in the giant quasar 4C 34.47. *ApJ*, 336:601–605, January 1989.
- R. D. Blandford. Quasar jets and their fields. In *Astronomy, physics and chemistry of H_3^+* , pages 811–+, February 2000.
- B. J. Burn. On the depolarization of discrete radio sources by Faraday dispersion. *MNRAS*, 133:67–+, 1966.
- R. G. Conway, B. J. Burn, and J. P. Vallée. Measurements of structure and polarization of 72 sources from the 4C catalogue. *A&AS*, 27:155–+, February 1977.
- J. Dennett-Thorpe, A. H. Bridle, R. A. Laing, and P. A. G. Scheuer. Asymmetry of jets, lobe size and spectral index in radio galaxies and quasars. *MNRAS*, 304:271–280, April 1999.
- J. Dennett-Thorpe, A. H. Bridle, P. A. G. Scheuer, R. A. Laing, and J. P. Leahy. Asymmetry of jets, lobe length and spectral index in quasars. *MNRAS*, 289:753–765, August 1997.
- I. Fernini. Fanaroff-Riley II Radio Galaxies and Quasars: The Depolarization Test. *AJ*, 122:83–92, July 2001.
- I. Fernini, J. O. Burns, J. P. Leahy, and J. P. Basart. Depolarization asymmetry in the quasar 3C 47. *ApJ*, 381:63–71, November 1991.
- I. Fernini, J. P. Leahy, J. O. Burns, and J. P. Basart. Depolarization Asymmetry in the Quasar 3C 47. *BAAS*, 22:800–+, March 1990.
- S. T. Garrington and R. G. Conway. The interpretation of asymmetric depolarization in extragalactic radio sources. *MNRAS*, 250:198–208, May 1991.
- S. T. Garrington, R. G. Conway, and J. P. Leahy. Asymmetric depolarization in double radio sources with one-sided jets. *MNRAS*, 250:171–197, May 1991.
- S. T. Garrington, J. P. Leahy, R. G. Conway, and R. A. Laing. A systematic asymmetry in the polarization properties of double radio sources with one jet. *Nature*, 331:147–149, January 1988.
- D. Golombek, G. K. Miley, and G. Neugebauer. IRAS observations of radio galaxies. *AJ*, 95:26–36, January 1988.

- J. A. Goodlet and C. R. Kaiser. The depolarization properties of powerful extragalactic radio sources as a function of cosmic epoch. *MNRAS*, 359:1456–1468, June 2005.
- A. Hewitt and G. Burbidge. A revised optical catalog of quasi-stellar objects. *ApJS*, 43:57–158, May 1980.
- L. C. Ho and C. Y. Peng. Nuclear Luminosities and Radio Loudness of Seyfert Nuclei. *ApJ*, 555:650–662, July 2001.
- J. R. A. Hooimeyer, P. D. Barthel, R. T. Schilizzi, and G. K. Miley. Monitoring of the superluminal quasar 4C 34.47. *A&A*, 261:1–4, July 1992.
- W. J. Jägers, G. K. Miley, W. J. M. van Breugel, R. T. Schilizzi, and R. G. Conway. Radio observations of the giant quasar 4C 34.47. *A&A*, 105:278–283, January 1982.
- K. I. Kellermann, R. Sramek, M. Schmidt, D. B. Shaffer, and R. Green. VLA observations of objects in the Palomar Bright Quasar Survey. *AJ*, 98:1195–1207, October 1989.
- K. I. Kellermann, R. A. Sramek, M. Schmidt, R. F. Green, and D. B. Shaffer. The radio structure of radio loud and radio quiet quasars in the Palomar Bright Quasar Survey. *AJ*, 108:1163–1177, October 1994.
- R. A. Laing. The sidedness of jets and depolarization in powerful extragalactic radio sources. *Nature*, 331:149–151, January 1988.
- J. P. Leahy. Small-scale variations in the Galactic Faraday rotation. *MNRAS*, 226:433–446, May 1987.
- R. Liu and G. Pooley. Spectral index and depolarization asymmetry in powerful radio sources. *MNRAS*, 249:343–351, March 1991a.
- R. Liu and G. Pooley. The correlated radio and optical asymmetries of powerful radio galaxies. *MNRAS*, 253:669–674, December 1991b.
- B. Q. McGimsey and H. R. Miller. Historical lightcurves of three QSOs. *A&AS*, 31:147–+, February 1978.
- G. K. Miley and J. S. Miller. Relations between the emission spectra and radio structures of quasars. *ApJ*, 228:L55–L58, March 1979.
- L. Miller, J. A. Peacock, and A. R. G. Mead. The bimodal radio luminosity function of quasars. *MNRAS*, 244:207–213, May 1990.
- G. Neugebauer, B. T. Soifer, and M. Rowan-Robinson. IRAS observations of active galaxies. In G. Giuricin, M. Mezzetti, M. Ramella, and F. Mardirossian, editors, *ASSL Vol. 121: Structure and Evolution of Active Galactic Nuclei*, pages 11–19, 1986.

- G. Paturel and C. Petit. Comparaison LEDA/SIMBAD octobre 2002. *LEDA (2002)*, 2002.
- T. J. Pearson and J. A. Zensus. Superluminal radio sources - Introduction. In J. A. Zensus and T. J. Pearson, editors, *Superluminal Radio Sources*, pages 1–11, 1987.
- P. A. G. Scheuer and A. C. S. Readhead. Superluminally expanding radio sources and the radio-quiet QSOs. *Nature*, 277:182–185, January 1979.
- J. T. Stocke, S. L. Morris, R. J. Weymann, and C. B. Foltz. The radio properties of the broad-absorption-line QSOs. *ApJ*, 396:487–503, September 1992.
- B. J. Wills and I. W. A. Browne. Relativistic beaming and quasar emission lines. *ApJ*, 302:56–63, March 1986.

List of Tables

1	The typical resolutions θ_{HPBW} of the observations in arcseconds.	18
2	RA and Dec positions of the centers of target and calibration sources in 1950 (FK4) and 2000 (FK5) coordinates.	19
3	Important values used by calibration.	21
4	Integration times with theoretical noise and the maximum sensitivity limit achievable for each observation	22
5	Observational parameters.	24
6	Core strength comparisons.	26
7	Spectral indices at different locations.	30
8	RM values at specific locations.	39
9	DP values at different areas.	41

List of Figures

1	Cygnus-A	8
2	The manifestation of three types of polarization	9
3	Diagram of the Faraday effect	10
4	Spectra of eight types of AGN	11
5	Two images where the jets of the radio sources can be seen. On the left side an image of Radio Galaxy Cygnus A and on the right side the Quasar 3C175 taken from the 3C catalogue of Alan Bridle.	13
6	Sketch of the source and a magneto-ionic medium around the source demonstrating the Faraday screen which can cause the depolarization asymmetry. D is the diameter of the screen, a the radius and θ the angle to the line of sight.	14
7	Total intensity contour plot by Jägers et al. 1981.	15
8	An example uv-plot of an observation of 4C34.47 taken with L-band B-array. X-axis is the baseline length (in $k\lambda$), Y-axis is the flux (in Jansky's).	21
9	Contour plots of the four images. The contour levels are RMS (table (5)) times 3, 6, 9, 12, 18, 24, 48, 96, 192 $mJy \text{ Beam}^{-1}$. The first contour represents 3σ detection. From top left to bottom right: High resolution 20cm image (A1), Low resolution 20cm image (A3), High resolution 6cm image (A4), Low resolution 6cm image (C12).	25
10	Radio contours of 6 cm total intensity map of 3C 47 plotted over a greyscale of the depolarization ratio made by Fernini et al. [1991].	27
11	Combined 1.4 GHz image of two different resolution maps, A1 (see figure (9a)) and A3 (see figure (9b)). The FWHM of the clean beam is 7.5×7.5 in arcseconds. Contour levels are $0.25 \times$ 4, 6, 8, 10, 12, 14, 16, 18, 20, 25, 30, 40, 80, 160, 320 $mJy/Beam$.	28

12	Combined 5 GHz image of two different resolution maps, A4 (see figure (9c)) and C12 (see figure (9d)). The FWHM of the clean beam is 7.5 x 7.5 in arcseconds. Contour levels are 0.109 * 4, 6, 8, 10, 12, 14, 16, 18, 20, 25, 30, 40, 80, 160, 320 mJy/Beam. . . .	29
13	Gray scale representation of the spectral index between 1.4 GHz and 5 GHz with superimposed contours of total intensity. . . .	31
14	Contour map of the total intensity with polarization intensity and E-vectors overlaid at different frequencies. (a) 1452.4 MHz (b) 1502.4 MHz (c) 4885.1 MHz (d) 4835.1 MHz.	33
15	Contour map of the total intensity with linear polarization degree and E-vectors overlaid at different frequencies. (a) 1452.4 MHz (b) 1502.4 MHz (c) 4885.1 MHz (d) 4835.1 MHz.	34
16	Total intensity contour maps of north and south side of both IFs of A4, with linear polarization degree and E-vectors overlaid. (a) North lobe at 4872.6 MHz (b) North lobe at 4822.6 MHz (c) South jet + lobe at 4872.6 MHz (d) South jet + lobe at 4822.6 MHz.	35
17	Polarization intensity and angle plotted over a contour map of the southern hot spot of observation A3. Intermediate frequency at 1.4524 GHz.	37
18	Polarization intensity and angle plotted over a contour map of the southern hot spot of observation A3. Intermediate frequency at 1.5024 GHz. Note the small rotation with respect to the other 20 cm IF (figure 17).	37
19	Polarization intensity and angle plotted over a contour map of the southern hot spot of observation A4. Intermediate frequency at 4.8726 GHz.	38
20	Polarization intensity and angle plotted over a contour map of the southern hot spot of observation A4. Intermediate frequency at 4.8226 GHz. The 6 cm rotation difference is substantially smaller than at 20 cm.	38
21	Histogram plots of circular polarization of 4C34.47. Plot (a) shows the V-polarization of 1452.4 MHz image and (b) of the 4885.1 MHz image.	40
22	Dependence of the jet velocity to the angle at a flux ratio of $S_j/S_{cj}=24$	46
23	Dependence of the flux ratio of S_j/S_{cj} versus the angle at a relativistic speed of 0.9c	47